Bulletin of the Seismological Society of America, Vol. 100, No. 5A, pp. 2143–2162, October 2010, doi: 10.1785/0120080318

Hybrid Broadband Ground-Motion Simulation Using Scattering Green's Functions: Application to Large-Magnitude Events

by Banu Mena, P. Martin Mai, Kim B. Olsen, Matthew D. Purvance, and James N. Brune

Abstract We calculate near-source broadband (0–10 Hz) seismograms by combining low-frequency three-dimensional (3D) finite-difference seismograms (0–0.5 Hz) computed in a 3D velocity model using site-specific scattering Green's functions for random, isotropic scattering media. The scattering Green's functions are convolved with a slip-rate function to form local scattering operators (scatterograms), which constitute the high-frequency scattered wave field. The low-frequency and high-frequency scatterograms are then combined in the frequency domain to generate broadband waveforms. Our broadband method extends the Mai *et al.* (2010) approach by incorporating dynamically consistent source-time functions and accounting for finite-fault effects in the computation of the high-frequency waveforms. We used the proposed method to generate broadband ground motions at 44 sites located 5–100 km from the fault, for M_w 7.7 earthquake scenarios (TeraShake) on the southern San Andreas fault, which include north-to-south, south-to-north, and bilateral rupture propagation from kinematic and spontaneous dynamic rupture models. The broadband ground motions computed with the new method are validated by comparing peak ground acceleration, peak ground velocity, and spectral acceleration with recently proposed ground-motion prediction equations (GMPEs). Our simulated ground motions are consistent with the median ground motions predicted by the GMPEs. In addition, we examine overturning probabilities for 18 precariously balanced rock sites (PBR). Our broadband synthetics for the M_w 7.7 TeraShake scenarios show no preferred rupture direction on the southern San Andreas fault but are inconsistent with the existence of PBRs at several of the sites analyzed.

Introduction

The southern part of the San Andreas fault has not experienced a large earthquake since 1690, and the accumulated tectonic strain may be capable of generating up to an M_w 7.7 earthquake (Sieh and Williams, 1990). In an effort to estimate the ground motions resulting from such an event, Olsen *et al.* (2006, 2008) simulated low-frequency wave propagation using a three–dimensional (3D) finite-difference method. Two sets of simulations were performed based on kinematic (TeraShake-1, or TS1) and dynamic (TeraShake-2, or TS2) source descriptions. Due to computational constraints, the TeraShake simulations resolved the ground motions at frequencies less than 0.5 Hz. However, the frequency range of engineering interest extends at least up to 10 Hz, highlighting the necessity to develop realistic ground-motion simulation methods that are capable of reliably estimating both low-frequency and high-frequency amplitudes. A number of broadband simulation methods have been developed in recent years (Irikura and Kamae, 1994; Beresnev and Atkinson, 1997; Kamae *et al.*, 1998; Hartzell *et al.*, 1999; Pitarka *et al.*, 2000; Pulido and Kubo, 2004; Graves and Pitarka, 2004; Mena *et al.*, 2006; Pulido and Matsuoka, 2006; Liu *et al.*, 2006; Rodgers *et al.*, 2008) that combine deterministic low-frequency waveforms with stochastic high-frequency synthetic seismograms to generate ground motions in the frequency band of engineering interest (0–10 Hz). At frequencies less than about 1 Hz, these methodologies are capable of accurately predicting the amplitudes and phases of earthquake ground motions using 3D representations of Earth structure in conjunction with dynamic or dynamically compatible kinematic representations of the earthquake source. The high-frequency simulations (~1–10 Hz) typically use random vibration theory to account for the stochastic nature of near-source ground motions (Boore, 1983; Boore and Boatwright, 1984). The purely stochastic methods involve little physics in terms of parameterizing the earthquake rupture process and details of wave propagation. In contrast, recently developed methods incorporate the physics of seismic wave scattering at high frequencies ($f > \sim 1$ Hz) in the stochastic nature due to small-scale heterogeneities in the Earth's crust, the main cause for loss of coherency in the

high-frequency band and for seismic coda generation. For example, Hartzell *et al.* (2005) combined realistic small-scale heterogeneity in the source properties via a scattering function to calculate broadband time histories. Zeng *et al.* (1995) used scattering theory to generate high-frequency ground motions. Mai *et al.* (2010) use a site-specific scattering operator combined with finite-difference synthetics to generate hybrid broadband ground motions.

The approach by Mai *et al.* (2010) generates broadband synthetics by applying a simplified total slip-rate function calculated from the rupture model used for the low-frequency simulations. This limits their approach to smaller earthquakes (using a point-source approximation) or further distant sites where directivity effects become insignificant. Here, we extend the method of Mai *et al.* (2010) to account for finite-fault effects instead of applying a simplified point-source approach. In addition, we implement dynamically consistent source-time functions with varying slip values across the fault; those slip functions are then convolved with the high-frequency scattering operators. These improvements provide physically more realistic simulation capabilities for large, extended-fault ruptures for which the point-source approximation clearly breaks down. We also perform sensitivity tests by varying the scattering parameters, which are generally poorly constrained from data (see Appendix for details). Based on the resulting variations in ground-motion properties of engineering interest (e.g., peak ground acceleration, strong motion duration, and Arias intensity), we show that scattering parameters have to be chosen within a limited range of values in order to obtain realistic representations of the high-frequency wave fields.

We compute broadband waveforms for all seven TeraShake scenarios at 44 rock sites (Fig. 1). Eighteen of the

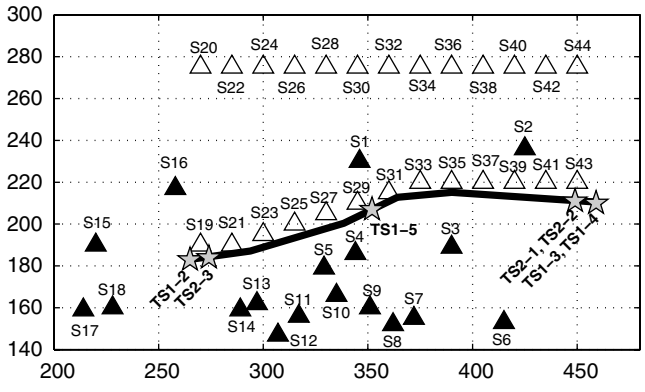

Figure 1. Broadband simulation area. Triangles show the locations of sites with respect to the 200-km-long, five-segment fault rupture (black line), where broadband synthetics have been computed. The black shaded triangles (sites from S01 to S18) are sites where PBRs are located and an overturning probability analysis has been carried out. The origin of the coordinate system (0, 0) is the left bottom corner of the TeraShake simulation area shown in figure 1 of Olsen and Brune (2008). The stars show the epicenters of the seven TeraShake scenarios.

44 rock sites have been chosen for analysis due to the presence of precariously balanced rocks (PBRs). PBRs are geologic features that are sensitive to strong ground shaking and could be toppled should the ground-motion amplitudes be sufficiently large. Thus, the existence of a PBR is an observation that the ground-motion amplitudes have not exceeded critical values at that particular site during the PBR residence time. Rock varnish microlaminations, in concert with terrestrial cosmogenic nuclide ages, have shown that a set of granitic PBRs in southern Nevada and California have been in place for over 10,000 years with no evidence of significant shape alteration (Bell *et al.*, 1998). Therefore evidence suggests that the PBRs near the southern San Andreas fault, where the San Bernardino Mountains and the Coachella segments have average recurrence intervals for large surface-rupturing events with surface rupture of approximately 150 years and 220 ± 13 years, respectively (Working Group on California Earthquake Probabilities, 1995), have been exposed to numerous earthquake cycles.

Purvance *et al.* (2008a) developed PBR fragility curves using numerical simulations and validated these fragilities through shake table experiments. They also demonstrated that the fragilities can be effectively parameterized as functions of the PBR geometrical parameters, the high-frequency ground-motion amplitude (PGA), along with a measure of the duration of the predominant acceleration pulse (parameterized as PGV/PGA ratio, where PGV is peak ground velocity). Thus broadband ground-motion estimates are required to quantitatively assess the overturning potentials of PBRs. Purvance *et al.* (2008a) present the PBR geometric parameters and their uncertainties of the selected PBRs and demonstrate methodologies to compare PBRs with deterministic and probabilistic seismic hazard estimates. Additionally, they show that the 2002 National Seismic Hazard Maps are inconsistent with the existences of numerous PBRs in southern California.

In our study, we use the PBR fragilities of Purvance *et al.* (2008a) to estimate the overturning probabilities when exposed to the broadband TeraShake ground motions. Previously, Olsen and Brune (2008) compared near-fault ground motions from the TeraShake simulations with PBR locations in an attempt to constrain the preferred rupture directions of past San Andreas events in the region. The current work thus expands and improves upon Olsen and Brune (2008) by providing quantitative comparisons between the PBR observations and the TeraShake ground motions by also including the high-frequency wave-field ground-motion contributions.

For validating the resulting ground-motion amplitudes, the PGAs and PGVs are compared with ground-motion prediction equations GMPEs. The applicability of our method for engineering design purposes is further validated by comparing spectral accelerations (SAs) at a range of periods against GMPEs. We utilize the GMPE of Choi and Steward (2005), as well as the NGA (Next Generation of Attenuation project) GMPE of Campbell and Bozorgnia (2008), which is

based on the most comprehensive ground-motion catalog assembled to date.

Broadband Synthetics for TeraShake Scenarios

The TeraShake simulations for M_w 7.7 scenario earthquakes on the southern San Andreas fault are described in Olsen *et al.* (2006, 2008). They approximated the fault geometry with five vertical, planar segments, reaching a total rupture length of 200 km and down-dip width of 15 km. Fault geometry and assumed epicenters for the seven scenarios are shown in Figure 1, along with the 44 rock sites where our broadband simulation method is applied. The four TS1 simulations used a kinematic description of the rupture based on the 2002 M_w 7.9 Denali earthquake source inversion of Oglesby *et al.* (2004), while the three TS2 simulations used a dynamic description of the rupture propagation inferred from the M_w 7.3 Landers earthquake (Peyrat *et al.*, 2001). Olsen *et al.* (2008) have found that TS1 and TS2 simulations produce similar spatial ground-motion patterns, but the TS2 peak ground motions were lower by a factor of 2–3 in parts of the Los Angeles basin. They attributed the lower TS2 ground motions to a more incoherent wave field generated by the more complex spontaneous ruptures, as compared to the simpler kinematic source descriptions. The TS1 scenarios differ from each other in the orientation of the assumed slip distribution and the direction of rupture propagation (see Fig. 1). The TS2 scenarios vary in the direction of rupture propagation and, in TS2-1, the occurrence of supershear rupture speeds. Table 1 summarizes the characteristics of the seven TeraShake scenarios.

Broadband Methodology

In an effort to compute realistic extended-fault, broadband synthetic seismograms, we deploy a hybrid approach in which low-frequency and high-frequency ground motions are computed separately and then combined. Low-frequency waveforms are calculated using a 3D finite-difference method, while the high-frequency synthetics are generated considering the scattered wave field due to a heterogeneous Earth crust. The low-frequency and high-frequency synthetics are then combined in the frequency domain using a Fourier domain approach that optimizes phase and amplitude matching at the intersecting frequency (Mai and Beroza, 2003; Mai *et al.*, 2010).

Generation of Low-Frequency Synthetics

A staggered-grid, velocity-stress finite-difference scheme is used to solve the 3D elastic equations of motion (Olsen, 1994). The accuracy of the solution is fourth order in space and second order in time. An explicit planar free-surface boundary condition colocated with the shear stresses (Gottschämmer and Olsen, 2001) is employed. Absorbing boundary conditions at the model edges are efficiently implemented using perfectly matched layers (Marcinkovich and Olsen, 2003). In addition, the coarse-grained implementation of memory variables for a constant-Q solid (Day and Bradley, 2001) is applied.

In this study, we make use of the TeraShake simulations (Olsen *et al.*, 2006, 2008) that simulate 4 min of wave propagation for frequencies up to 0.5 Hz. The velocities of the near-surface layers were truncated at 500 m/s due to computational limitations (Olsen *et al.*, 2008), and surface topography was neglected. The simulations used a 3D crustal structure, extracted as a subset of the Southern California Earthquake Center Community Velocity Model version 3.0 (Magistrale *et al.*, 2000; Kohler *et al.*, 2003).

Generation of High-Frequency Synthetics

Calculation of Scattering Green's Functions: Site-Specific Scattering Operators. In addition to direct, reflected, and refracted wave arrivals, small-scale heterogeneities in earth structure produce scattered waves. To simulate seismic wave scattering and quantify the high-frequency wave field due to small-scale heterogeneities, the isotropic scattering theory of Zeng *et al.* (1991) and Zeng *et al.* (1993) was used by Mai *et al.* (2010). This theory allows for the computation of the temporal decay of scattered wave energy, including all multiple-scattering contributions. Zeng *et al.* (1993) showed that the S-to-S-scattered wave field approximates the complete scattered wave field that includes scattering conversion between P and S waves shortly after the S arrival. The energy envelope of the S-to-S-scattered waves ($E(r, t)$) is computed using the scattered wave energy equation from Zeng *et al.* (1991), given by

Table 1
Overview of the Seven TeraShake Scenarios (Olsen *et al.*, 2006, 2008)

Scenario	Rupture Direction	Slip Distribution	Average Slip (m)	Maximum Slip (m)	V_r (km/s)	τ (s)
TS1-2	NW to SE	Kinematic source description based on M 7.9 Denali	4.0	9.9	3.3	3.2
TS1-3	SE to NW	Kinematic source description based on M 7.9 Denali	4.0	9.9	3.3	3.2
TS1-4	SE to NW	Kinematic source description based on M 7.9 Denali, lateral mirror of TS1.3	4.0	9.9	3.3	3.2
TS1-5	bilateral	Kinematic source description based on M 7.9 Denali	4.0	9.9	3.3	3.2
TS2-1	SE to NW	Dynamic source description based on M 7.3 Landers	4.2	9.2	3.4	3.2
TS2-2	SE to NW	Dynamic source description based on M 7.3 Landers	4.2	8.2	3.3	3.2
TS2-3	NW to SE	Dynamic source description based on M 7.3 Landers	4.2	8.5	2.9	3.2

$$E(\vec{r},t) = \frac{\delta(t-\frac{r}{\beta})e^{-\eta\beta t}}{4\pi\beta r^2} + \sum_{n=1}^{2} E_n(\vec{r},t) + \int_{-\infty}^{\infty} \frac{e^{i\Omega}}{2\pi} d\Omega \int_0^{\infty} \frac{(\frac{\eta_s}{k})^3 [\tan^{-1}(\frac{k}{\eta+i\Omega/\beta})]^4 \sin(kr)}{2\pi^2\beta r[1-\frac{\eta_s}{k}\tan^{-1}(\frac{k}{\eta+i\Omega/\beta})]} dk. \quad (1)$$

Equation (1) is the integral solution for the fundamental wave energy equation (Zeng *et al.*, 1991, equation 4a) computed using Laplace transformation in time and spatial Fourier transformation. $i\Omega$ denotes the Fourier transform solution with respect to time, and k is the wave-number. η_s is the scattering coefficient for elastic attenuation, η_i is the absorption coefficient for anelastic attenuation, and $\eta = \eta_i + \eta_s$. Anelastic attenuation (η_i) is replaced by $Q(f) = Q_0 f^n$ in equation 1, unless a constant Q is assumed. η denotes the total S-wave attenuation coefficient that mainly controls the exponential decay of the S-wave coda. Our choice of elastic (η_s) and anelastic ($\eta_i = Q_0 f^n$) attenuation based on sensitivity tests and observational studies is explained in the Appendix. β is the average S-wave velocity between source and receiver, and r is the source receiver distance. The first term in equation 1 denotes the direct arrival, the second term is the singly ($n = 1$) and doubly ($n = 2$) scattered energy, and the third term comprises the multiple scattering contributions. Green's functions for direct S waves use a $1/R$ geometrical spreading (equation 1). Crustal and Moho reflections are not considered. Because the scattered waves arrive at a given site from all directions within the scattering volume surrounding the source and receiver, Zeng *et al.* (1991) assumed isotropic radiation for the direct waves in the derivation of equation 1. Effects of the source radiation pattern are therefore averaged out for the high-frequency scattered waves.

In the numerical implementation, the computed coda envelope (equation 1) is filled with correspondingly scaled random scattering wavelets; the resulting time series thus represents a scattering Green's function. This theory holds for body waves, while scattered surface waves are not considered. Such approximation is justified in our current study because we are dealing with near-field simulations, where surface waves have not yet developed (at close sites) or are rather small (at far sites). Near-surface effects that control ground shaking at higher frequencies (e.g., site-specific attenuation in the upper layers at frequencies above $f_{\max}$) are modeled with a site-kappa coefficient (κ); the choice of κ is examined in the Appendix.

Calculation of Scatterograms: Convolution with a Source-Time Function. The calculation of high-frequency local scattering operators (scatterograms) follows Mai *et al.* (2010). P-wave and S-wave phase arrivals at each site are computed using a 3D ray-tracing algorithm (Hole, 1992). Scattering Green's functions are generated for an elementary source (1 cm of slip occurring on a 1 km × 1 km fault patch). The scattering Green's functions are then convolved with the slip-rate function at that point on the fault, forming a scatterogram. The source-time function (STF) can either be computed based on the temporal slip evolution of the chosen source rupture model for the low-frequency simulation or by assuming a simplified source-time function. Here we further build on the method by Mai *et al.* (2010) by testing various STFs shown in Figure 2, as well as the sensitivity of the resulting ground motions to these functions. Canonical slip-rate functions (boxcar, triangular, or trapezoidal functions) can be applied for simplicity, but source-time functions compatible with rupture dynamic are generally preferable.

There have been efforts to produce simplified yet physically realistic STFs that are relatively easy to parameterize while still being consistent with rupture dynamics. However, to our knowledge, the use of these STFs in high-frequency ground-motion simulation has not been investigated. In our study, we implement the analytical solution for the regularized Yoffe function (Tinti *et al.*, 2005), the slip-rate function used by Liu *et al.* (2006), and the slip-rate function developed by Dreger *et al.* (2007). Tinti *et al.* (2005) proposed the Yoffe function (referred to as Yoffe-STFhereafter) as a dynamically consistent STF for kinematic rupture modeling to facilitate the dynamic interpretation of kinematic slip models. Liu *et al.* (2006) constructed the slip-rate function (referred to as Liu-STF hereafter) motivated by the results of dynamic rupture modeling of Guatteri *et al.* (2004). Dreger *et al.* (2007) proposed the so-called ζ—STF (referred to as Dreger-STF hereafter), which is compatible with slip functions of spontaneous dynamic rupture models (e.g., Guatteri *et al.*, 2003).

To examine the influence of these slip-rate functions on the scatterogram, we compare coda waves convolved with the boxcar-STF, the triangular-STF, the Yoffe-STF, the Liu-STF, and the Dreger-STF. Both the traditionally used STFs (boxcar-STF, triangular-STF) and the three dynamically consistent STFs (Yoffe-STF, Liu-STF, Dreger-STF) show very distinctive features (Fig. 2a,b), particularly significant in their spectra (Fig. 2c). The scatterograms (scattering Green's functions convolved with the respective STFs) are similar in shape and amplitude, but their amplitude spectra show significant differences for frequencies above 1 Hz, revealing a strong dependence of the spectral shape to the STF pulse shape. The acceleration spectra of the scatterogram convolved with the boxcar function show the typical flat acceleration spectra at frequencies above the corner frequency but have significantly lower amplitudes than the other scatterograms. The acceleration spectrum of coda convolved with triangular-STF does not show the expected flat acceleration spectra but instead has a continuous fall-off starting at very low frequencies (below 1 Hz). The Yoffe-STF generates spectral holes above 2 Hz due to the source spectrum of the Yoffe function (Fig. 2c). However seismic recordings usually do not show such spectral holes. Convolution with Liu-STF generates a scalloped spectral shape with a flat level in acceleration spectra for frequencies less than 1 Hz, followed by a very steep fall-off causing a loss of high-frequency energy above 1 Hz (see Fig. 2c for the sudden fall-off of the Liu-STF spectra above 1 Hz). Note also that the chosen pulse

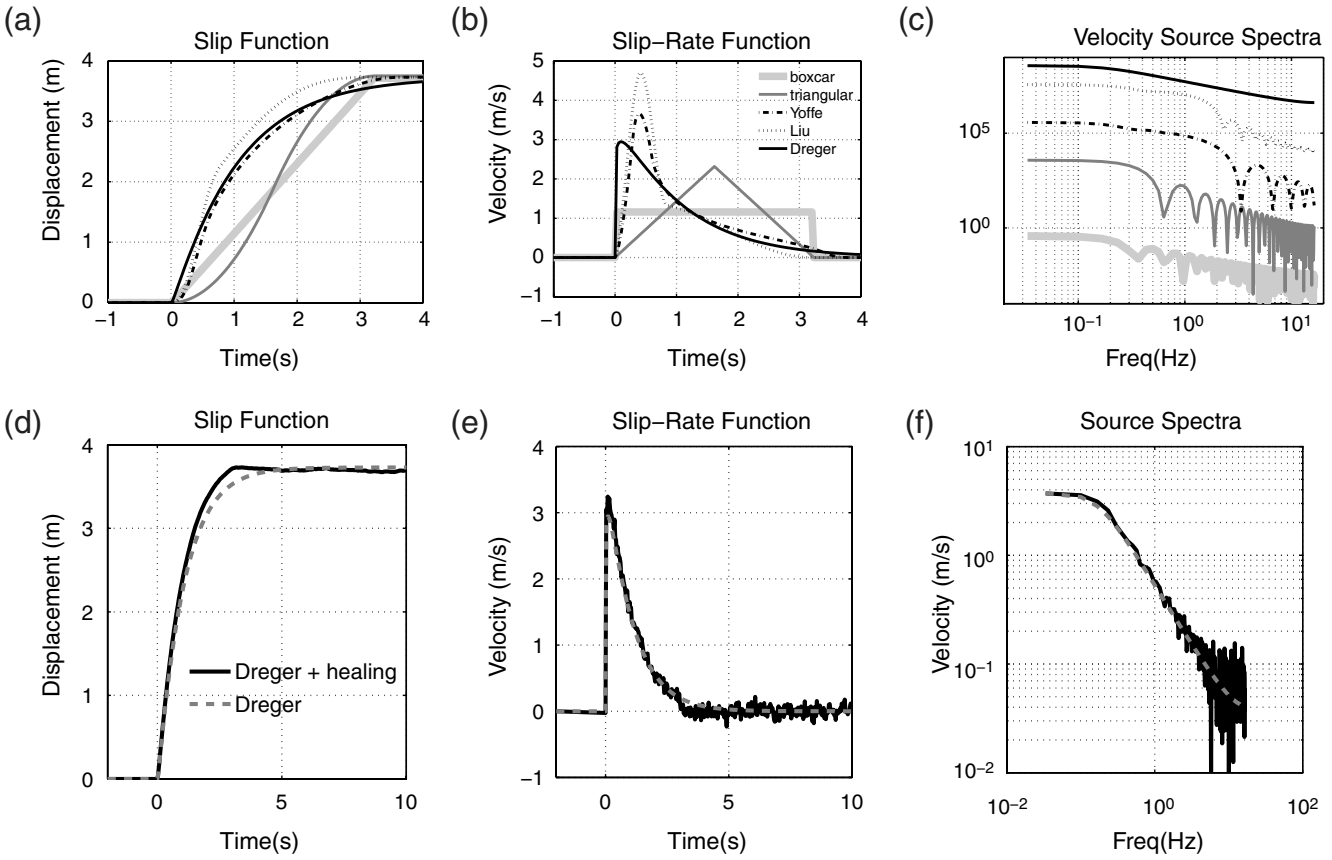

Figure 2. Overview of source-time functions analyzed in our study. a) Slip-time functions, b) slip-rate functions, and c) velocity spectra of boxcar-STF, triangular-STF, Yoffe-STF, Liu-STF, and Dreger-STF (offset by an arbitrary value for clarity of plotting). The original Dreger-STF (dashed gray line) is compared with the improved Dreger-STF (solid black line) in terms of (d) slip history, (e) slip-rate history, and (f) velocity spectra.

width of the Liu-STF strongly affects the shape of the spectra. The amplitude spectrum of the Dreger-STF neither contains spectral holes nor abrupt changes at lower frequencies (Fig. 2c). More importantly, it has the favorable attribute of a smooth spectrum that generates a flat-level acceleration spectrum beyond the corner frequency. The overall shape and particularly the rapid rise time of the dynamic slip velocity functions are well approximated by the Dreger-STF (Dreger *et al.*, 2007). The functional form of the Dreger-STF is given as

$$s(t,\tau,\zeta) = t^{\zeta} e^{-t/\tau}, \tag{2}$$

where τ is the pulse width and ζ (ranging between 0 and 1) defines the sharpness of the beginning of the time function and controls the high-frequency spectral decay rate. However, healing of slip is not included in the original parameterization, and we therefore modify the Dreger-STF by adding a healing phase of short duration. The parameterization of the modified Dreger-STF is then given as

$$s(t,\tau,\zeta) = \begin{cases} te^{-t/\tau} & 0 \le t \le n\tau \\ t^{\zeta} e^{-n} - \frac{t^{\zeta+1} e^{-n}}{(1-n)\tau} & n\tau < t < \tau \end{cases}. \tag{3}$$

In our calculations, we used $\zeta = 0.2$, as advised in Dreger *et al.* (2007) based on comparisons with the dynamic simulations. n is some percentage of the rupture duration that defines the onset of pulse healing and was taken as 0.9 in the simulations in this paper. The amplitude of the Dreger-STF, $s(t,\tau,\zeta)$, is scaled accordingly to match the final slip value at the respective subfault. The resulting slip-rate function is smooth, and so is its amplitude spectrum; however, seismic data inevitably reveal that observed slip-rate functions contain short-period variations and hence reflect source complexity. To emulate this source variability, we added a small amount of random white noise to the Dreger-STF. Numerical experiments show that for noise levels of 10% or more, peak slip rates in the STF time-series are significantly affected and the approximate $1/f$ decay is strongly degraded. We thus chose to add 5% random white noise, which maintains the overall time-domain and frequency-domain characteristics of the slip-rate function but contributes realistic small-scale variability to the STF. The slip functions, slip-rate functions, and the source spectra of the original Dreger-STF (as proposed in Dreger *et al.*, 2007) and the improved Dreger-STF are plotted in Figure 2d,e,f.

Extended Fault Approximation. The scattering Green's functions are generated for a unit rupture-area (1 km× 1 km) assuming a uniform displacement of 1 cm on the rupture surface, and therefore the STF needs to be scaled to the magnitude of the target event. Mai *et al.* (2010) proposed a constant scaling factor applied to either the scattering Green's functions or the STF. This factor accounts for the total rupture assuming point-source radiation for the high-frequencies and does not correspond to a finite-fault source. For larger events, such as the M_w 7.7 TeraShake scenarios, a point-source assumption is not appropriate, and an alternative approach is needed to generate realistic scattering contributions.

We therefore divide the fault area into a number of subfaults. The summation of the scattering Green's functions emitted at each subfault is similar to the empirical Green's function method of Irikura and Kamae (1994), which adds the contribution of the individual subfaults to obtain the total ground motion at the specified site as follows:

$$A(t) = \sum_{i=1}^{N^2} (r/r_i)\mathrm{STF}(t - t_i) * C(sgf(t)). \quad (4)$$

In equation 4, r is the hypocentral distance, r_i is the distance from the observation point to the i-th subfault, $sgf(t)$ is the scattering Green's function, C is the stress drop ratio between the small and large event, N^2 is the number of subfaults to be summed up to generate the large earthquake ground motion, and the asterisk indicates the convolution. STF(t) is the source-time function, and $A(t)$ is the resultant high-frequency ground motion.

The level of the high-frequency spectral amplitude, relative to seismic moment, is reached according to the following scaling law (Irikura, 1986).

$$\frac{M_0}{m_0} = CN^3. \quad (5)$$

Here, M_0 and m_0 correspond to the seismic moments for the large (the finite-fault in our study) and small events (subfaults in our study), respectively, and N and C are the ratio of the corresponding fault dimensions and stress drops between the large and small events, respectively.

The scattering Green's functions for the unit-size, unit-slip earthquake correspond to an M_w 3.7 event with a seismic moment of 3.3×10^{14} Nm. The target M_w 7.7 TeraShake ruptures have a seismic moment of 4×10^{20} Nm with a rupture area of $L = 200$ km and $W = 15$ km.

The stress drop ratio C is found assuming scale-independent stress drop, with static stress drop being proportional to $M_0/(LW)^{3/2}$ for the large event and $m_0/(lw)^{3/2}$ for the small event (Irikura and Kamae, 1994). Finally, N^2 in equation 5 is estimated as $nx \times nz = 3000$, where nx and nz are the number of subfaults along strike and dip directions respectively. The TeraShake fault area (200 km × 15 km) is divided into 200 by 15 subfaults along strike and dip directions, respectively, in agreement with the scattering Green's function fault area of 1 km^2.

The Dreger-STF is used for STF($t - t_i$) in equation 4, where t_i accounts for the time delay for rupture propagation along the fault:

$$t_i = r_i/V_s + \xi_i/V_r, \quad (6)$$

where r_i is the distance from the observation point to the i-th subfault (same as in equation 4), ξ_i is the distance from the rupture nucleation point to the i-th subfault, and V_r is the rupture velocity. The slip duration for high frequencies (τ) in equation 3 is that of the target event and computed for an M_w 7.7 earthquake following the scaling relation of Somerville *et al.* (1999). Constant slip duration is used across the fault for our high-frequency simulations.

The spatial variability in slip across the fault is implemented by correspondingly scaling the STF($t - t_i$) at each subfault to reach the final slip value at the respective subfault. The final slip distributions for TS1 and TS2 simulations (Fig. 3) used in the high-frequency TeraShake simulations are taken from Olsen *et al.* (2006, 2008). We used constant rupture velocities to generate the high-frequency ground motions, taken as the average values from the low-frequency TeraShake rupture models (Table 1).

Combination of Low-Frequency and High-Frequency Synthetics: Hybrid Broadband Ground-Motion Generation

Finally, the low-frequency synthetics computed by 3D finite differences are combined with the site-specific scatterograms in the frequency domain using the optimization approach of Mai and Beroza (2003). This is a simultaneous amplitude and phase matching algorithm, searching for the optimum matching frequency within a specified frequency band to obtain minimum amplitude and phase mismatch between the low-frequency and high-frequency spectra. The optimized matching frequency is site specific and component specific, taking values within a preset search range. This approach prevents artificial spectral jumps or holes that may exist near the matching frequency where the low-frequency and high-frequency spectra are joined. In the present study, we search for the optimum matching frequency between 0.2–0.5 Hz because the low-frequency synthetics are limited to 0.5 Hz. Figure 4 displays a set of simulation results illustrating the site-specific selection of the matching frequency and corresponding waveforms.

Comparison with Ground-Motion Prediction Equations (GMPE)

We compare ground-motion parameters derived from our broadband simulations with the GMPE of Choi and Stewart (2005) and the recent NGA GMPE of Campbell and Bozorgnia (2008). The two GMPEs differ slightly from each

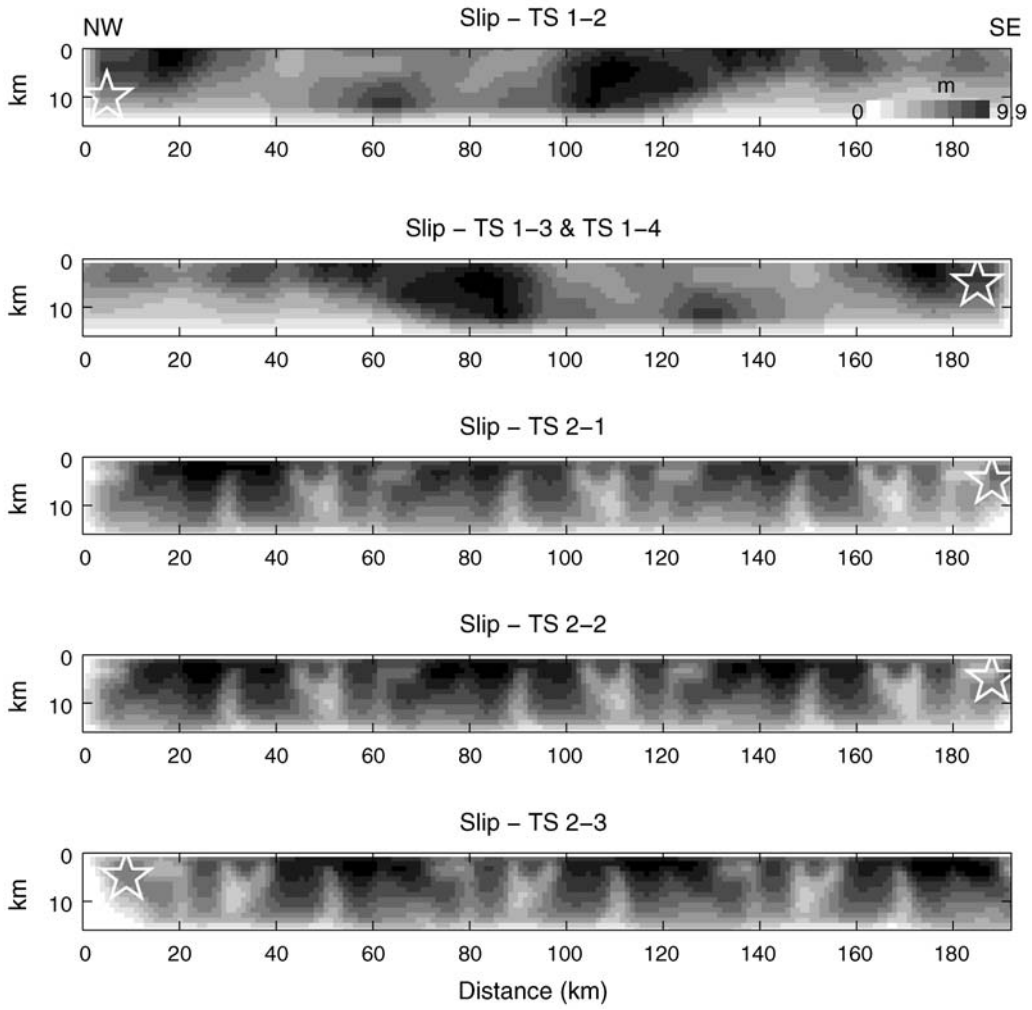

Figure 3. Final slip distribution for TeraShake-1 and TeraShake-2 simulations.

other in amplitude, and the Choi and Stewart (2005) relation decays more rapidly with distance than does the Campbell and Bozorgnia (2008) model, especially for PGA. PGA, PGV, and SA (for several periods and for 5% damping) comparisons with the empirical models are shown in Figures 5–10. The GMPE values are obtained for hard rock (the surface *S*-wave velocity used in the low-frequency rupture models). The geometric mean of the two horizontal components of ground motion is used throughout our GMPE comparisons. Because the estimated broadband ground motions for TS1-4 are very similar to those for TS1-3 due to similarity in rupture propagation (see Table 1), ground-motion comparisons for TS1-4 are not shown.

Although our simulations agree well with the median values for both models and generally fall within ± 1 standard deviation (σ), our simulations more strictly follow the distance decay of the Choi and Steward (2005) model (Fig. 5). To assess the level of fit between our simulations and the GMPEs, we compute the residuals at every site for each TS scenario. The residual at each site i is given as

$$r_i = \ln\left(\frac{PGA_{\text{model},i}}{PGA_{\text{simulated},i}}\right), \tag{7}$$

where $PGA_{\text{model},i}$ is the PGA prediction from the attenuation model and $PGA_{\text{simulated},i}$ is the value from our broadband simulations. A perfect match between the median empirical model and the broadband simulation would have $r_i = 0$, whereas a positive residual shows underprediction and a negative value shows an overprediction of the simulations with respect to the empirical model. Figure 11 shows the plot of PGA residuals versus distance, with the mean and standard deviation of the residuals listed, to evaluate the agreement with the GMPE of Choi and Stewart (2005). As seen from the plots for each TS scenario, most of the residuals fall within the range ± 0.5. The few sites that fall above or below ± 0.5 range are the ones subjected to full backward or strong forward directivity effects.

As seen from Figure 5 and Figure 11, site S21 for TS1-2, site S41 for TS1-3, sites S21, S33, S37, and S39 for TS1-5, sites S39 for TS2-1 and TS2-2, and site S25 for TS2-3 have PGA values higher than $+1\sigma$ value. All these sites are near-field

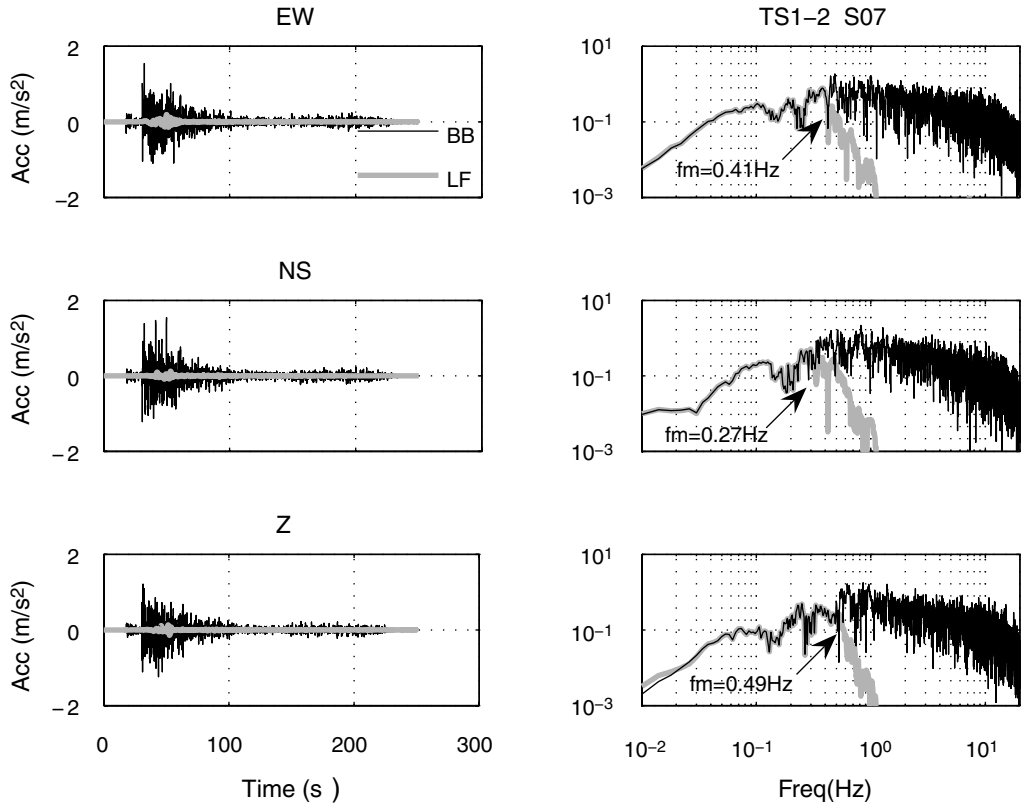

Figure 4. Example of low-frequency (gray color) and hybrid broadband (black color) acceleration synthetics (left) and corresponding Fourier amplitude spectra (right) from the TS1-2 scenario at station S07 for the east–west (EW), north–south (NS), and vertical (Z) components (from top to bottom). The matching frequencies (fm) found by the optimization approach are indicated by an arrow for each component.

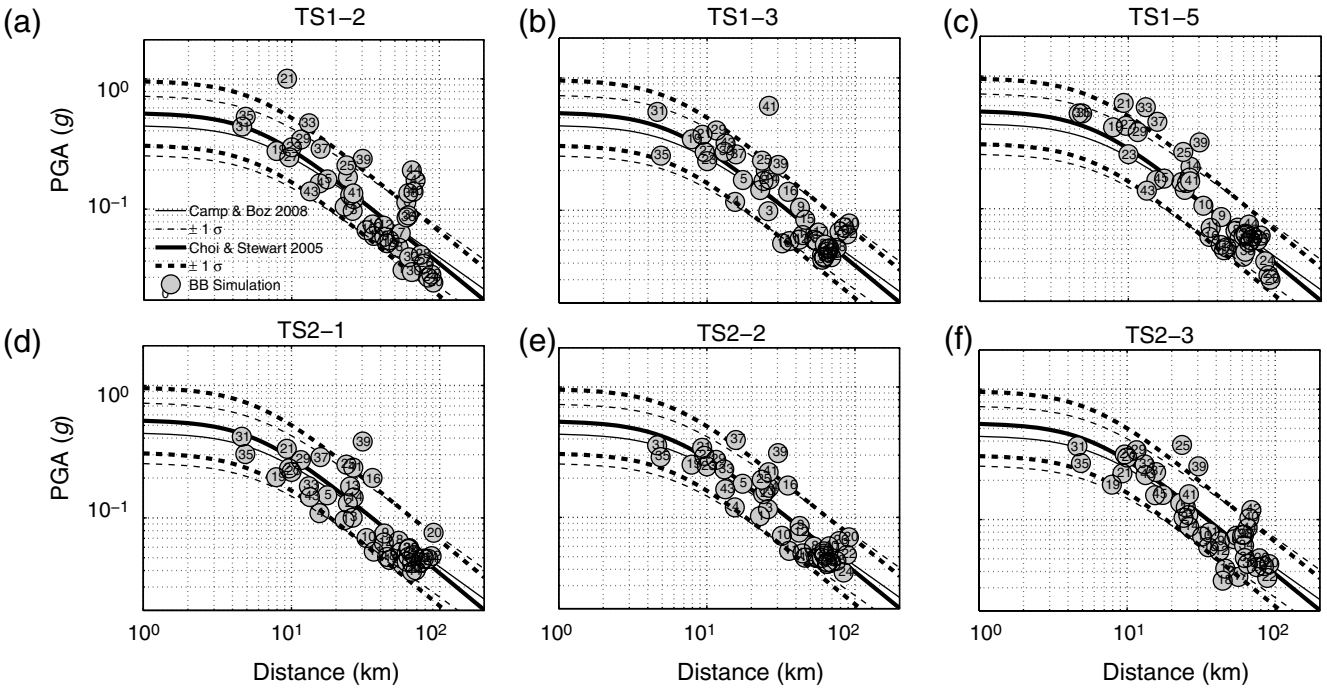

Figure 5. PGAs from broadband (BB) rock simulations at 44 sites (circles) calculated for (a) TS1-2, (b) TS1-3, (c) TS1-5, (d) TS2-1, (e) TS2-2, and (f) TS2-3 scenarios compared to values from Campbell and Bozorgnia (2008) and, Choi and Stewart (2005). The station numbers for each PBR site are plotted in circles (refer to Fig. 1 for the location of each site).

sites, near the epicenter of the respective scenario, and in the forward rupture direction. Additionally they are located very close to a large high slip patch (see Fig. 3). Therefore, these sites are not only subjected to global directivity effects (forward rupture direction) but also some local directivity effects (slip heterogeneity in this case). Similarly, the sites S15, S17, and S18 for northwest–southeast scenarios (TS1-2 and TS2-3) reveal strong backward directivity effects (low amplitudes, lower than -1σ) for TS2-3, whereas TS1-2 does not produce such low amplitudes at these locations. This is due to the existence of a large high slip patch at the northern edge of the fault for TS1-2 (close to sites S15, S17, and S18) that minimizes the backward directivity effects for this scenario but does not exist in TS2-3. Effects of global and local directivity and their consequences on near-field ground-motion variability are discussed in detail by B. Mena and P. M. Mai (personal comm., 2009).

The empirical attenuation relations do not distinguish between forward and backward directivity effects (which are abundant for the TeraShake simulations; see Olsen *et al.*, 2006, 2008) but represent an ensemble of both. Thus, it is not surprising that the SAs or PGAs at sites of backward and strong forward directivity fall above and below the median attenuation relations, respectively. Figure 11 shows that the mean of the PGA residuals between simulations and the GMPE are very close to zero for all TS simulations ($\sim \pm 0.05$). However, TS1 simulations have a negative mean (~ -0.05), indicating a minor overprediction, and TS2 simulations have a positive mean ($\sim +0.05$), indicating a minor underprediction from the mean. This shows that our broadband simulations using dynamic rupture models produce ground motions slightly lower than the simulations using kinematic rupture models, thus confirming the findings from Olsen and Brune (2008), which used the low-frequency simulations only.

Figures 7–10 show comparisons of SA computed for 5% damping at several periods ($T = 0.2$ s, $T = 0.3$ s, $T = 0.5$ s, $T = 0.75$ s). Additionally, we examine ensemble statistics of ground motions in terms of model bias $B(T_j)$, standard error, and 90% confidence intervals. The model bias $B(T_j)$ is computed as

$$B(T_j) = \frac{1}{N}\sum_{i=1}^{N} r_i(T_j). \tag{8}$$

The median model bias, the $\pm 1\sigma$ bound, and the 90% confidence intervals of SA are displayed in Figure 12, showing

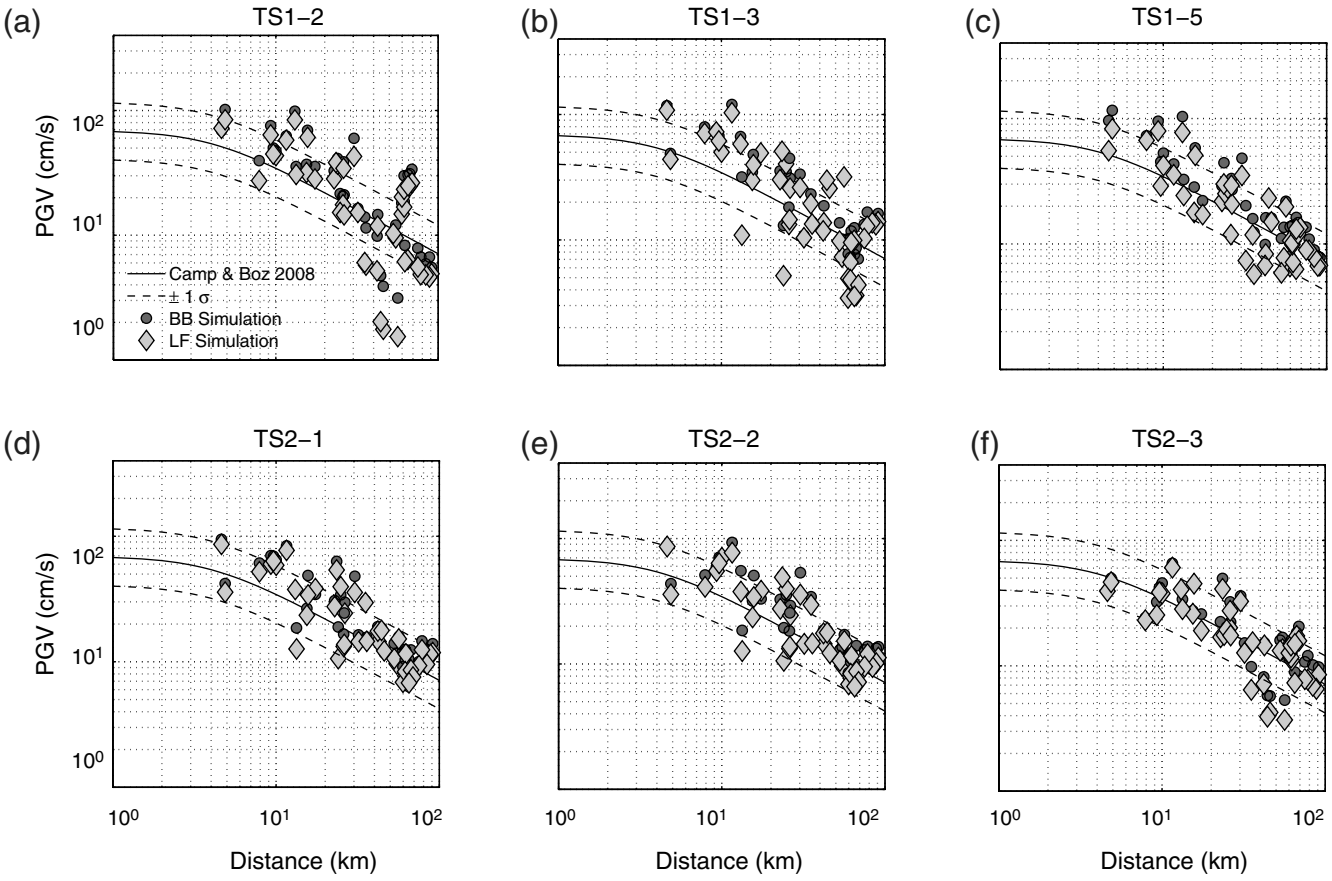

Figure 6. PGVs from broadband (BB) rock simulations (black circles) and from low-frequency rock simulations (open diamonds) calculated for (a) TS1-2, (b) TS1-3, (c) TS1-5, (d) TS2-1, (e) TS2-2, and (f) TS2-3 scenarios compared to the GMPE of Campbell and Bozorgnia (2008).

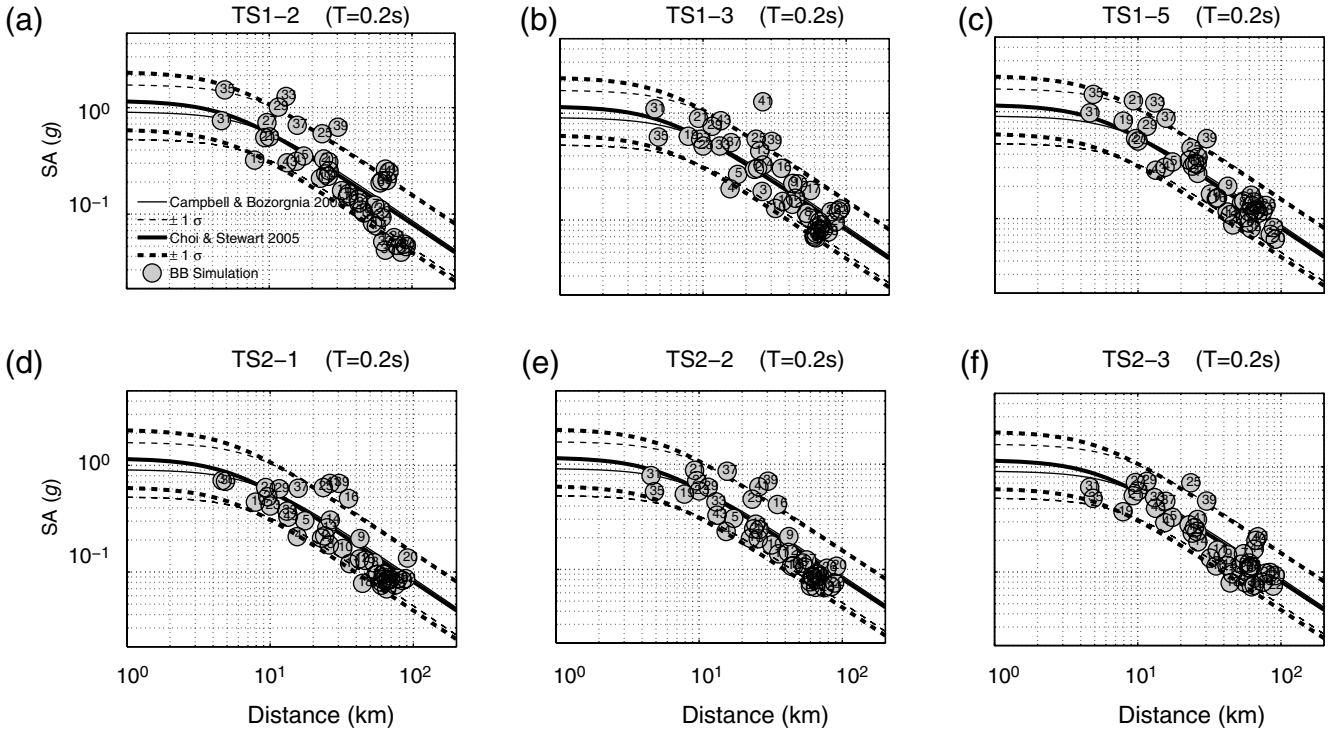

Figure 7. SAs for $T = 0.2$ s (elastic response spectra with 5% damping) calculated for (a) TS1-2, (b) TS1-3, (c) TS1-5, (d) TS2-1, and (e) TS2-3 scenarios compared with the GMPE of Campbell and Bozorgnia (2008).

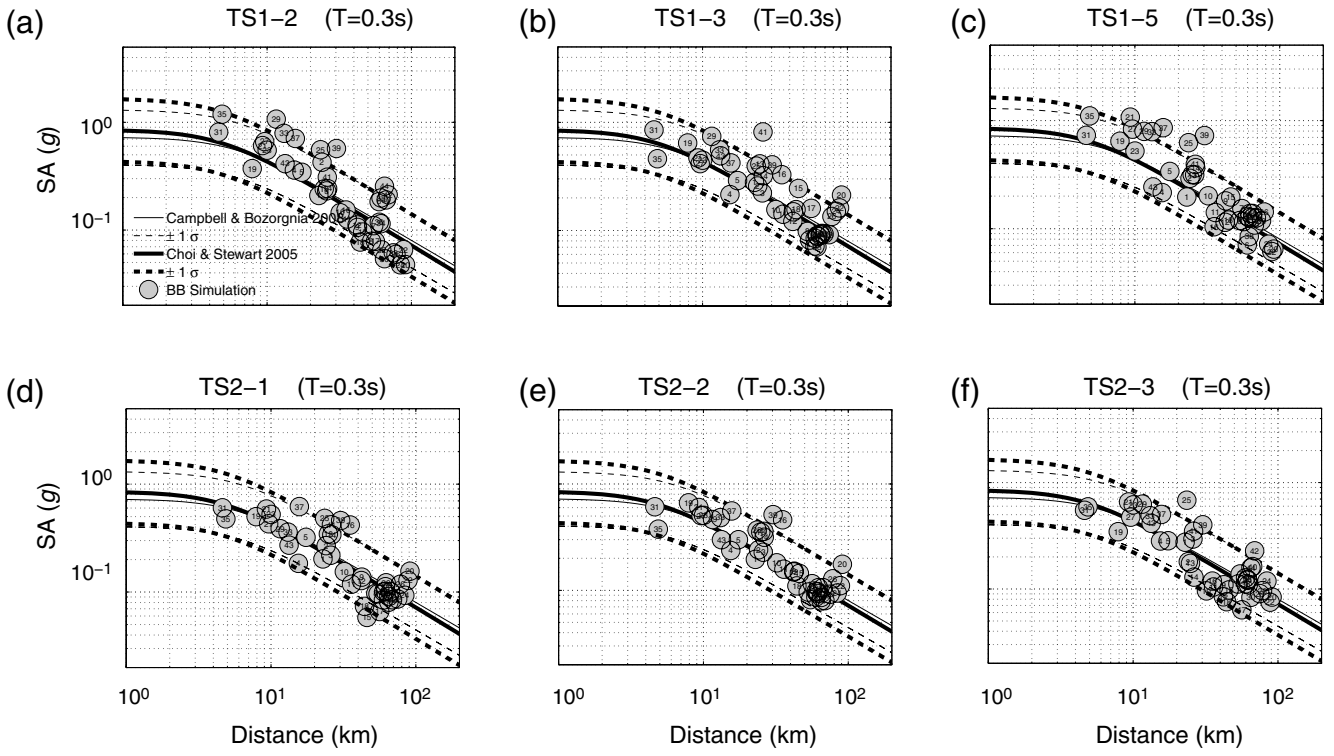

Figure 8. SAs for $T = 0.3$ s (elastic response spectra with 5% damping) calculated for (a) TS1-2, (b) TS1-3, (c) TS1-5, (d) TS2-1, and (e) TS2-3 scenarios compared with the GMPE of Campbell and Bozorgnia (2008).

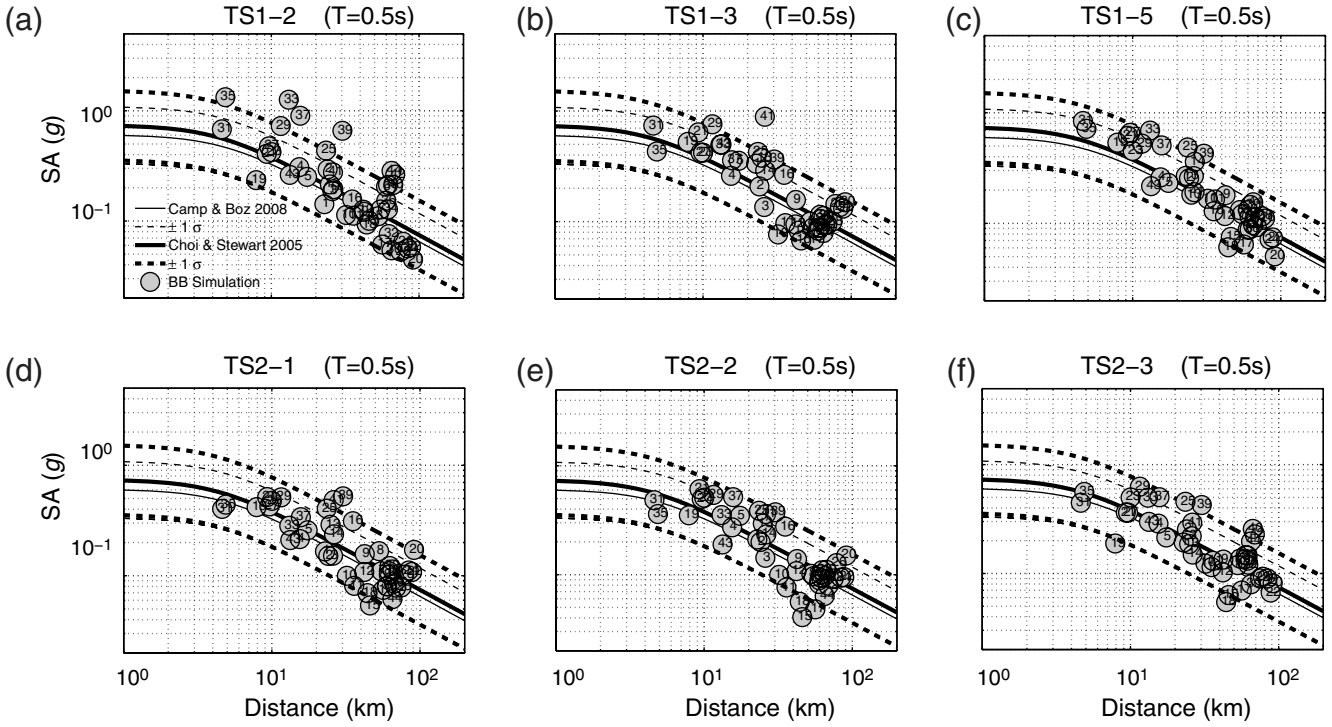

Figure 9. SAs for $T = 0.5$ s (elastic response spectra with 5% damping) calculated for (a) TS1-2, (b) TS1-3, (c) TS1-5, (d) TS2-1, and (e) TS2-3 scenarios compared with the GMPE of Campbell and Bozorgnia (2008).

that the median residuals fluctuate weakly around the zero-bias line, while the 90% confidence intervals are ~0.25 and $\pm 1\sigma$ bounds are ~0.5. The comparisons in Figure 11 and Figure 12 indicate that our simulation approach provides largely unbiased ground-motion estimates compared to the empirical GMPEs by means of computing realistic broadband

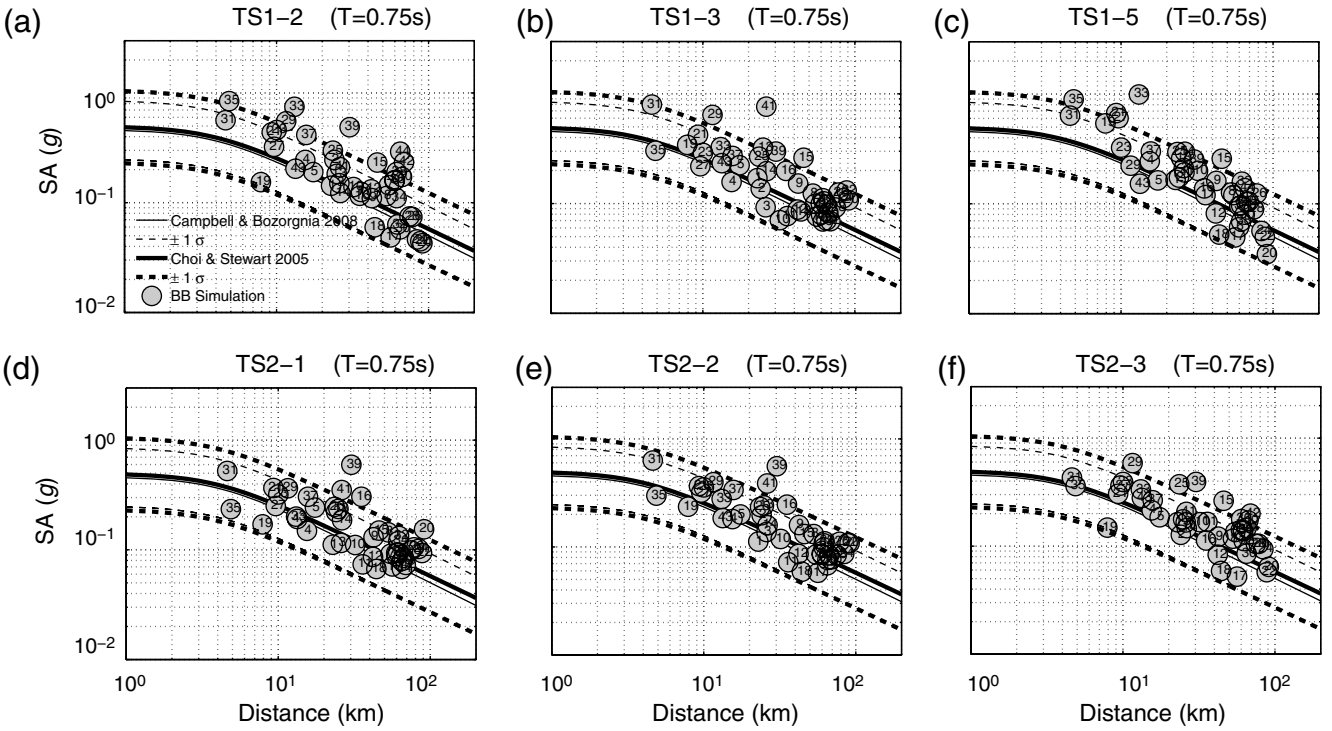

Figure 10. SAs for $T = 0.75$ s (elastic response spectra with 5% damping) calculated for (a) TS1-2, (b) TS1-3, (c) TS1-5, (d) TS2-1, and (e) TS2-3 scenarios compared with the GMPE of Campbell and Bozorgnia (2008).

time histories for complex ruptures embedded in a 3D heterogeneous crustal model.

To further assess the quality of our broadband synthetics, we examine the waveform and spectral characteristics. For all seven TeraShake scenarios; and, at most sites, we obtain smooth transitions between the high-frequency ground-motion amplitudes and the low-frequency synthetics at the matching frequency as illustrated in Figure 13a,c (note, there is no significant fall-off or jump at the matching frequencies). Occasionally, high-frequency amplitudes somewhat higher than the corresponding low-frequency spectral amplitude level (about a factor of 2) are obtained close to the matching frequency (Fig. 13b). The mismatch may be due to the assumption of isotropic radiation of the direct waves at high frequencies (Zeng *et al.*, 1993), while radiation pattern effects are fully included in the low-frequency simulation. A gradual, frequency-dependent transition from an isotropic to a source-dependent radiation pattern may potentially remove this small mismatch.

Site-Specific Amplification Factors at the 18 PBR Sites

Our broadband simulations are generated exclusively at rock sites, and the comparisons to the GMPE results in Figures 5–10 are done using the relatively large surface *S*-wave velocity of 3170 m/s used in the low-frequency finite-difference simulations. However adjustments may need to be included to account for lower shear-wave velocities in the near surface at the precarious rock sites. This is important because site amplification at these sites may increase the probability of overturning these precariously balanced rocks. To account for site-specific geologic conditions in the broadband simulations, we apply frequency-dependent amplification functions derived empirically by Borcherdt (1994), to the broadband synthetics at the 18 PBR sites. These functions have the form

$$F(x) = \left(\frac{V_{\text{site}}}{V_{\text{ref}}}\right)^{m_x}, \tag{9}$$

where V_{site} denotes the average shear-wave velocity in the top 30 m (V_{s30}) at the site of interest, V_{ref} corresponds to V_{s30} where the ground response is known, and m^x denotes an empirically determined factor that depends on both period and ground-motion level. Because the exponent m_x decreases as the reference PGA value increases, equation 9 also accounts for the nonlinear site response.

The reference site condition V_{ref} in this study is the surface shear-wave velocity in the 3D velocity-density model that is used in low-frequency simulations (3170 m/s at all selected sites), determined by the V_{s30} used in the low-frequency finite-difference simulations. Based on the work of Purvance *et al.* (2008b), the V_{s30} of the PBRs are generally around 760 m/s (which correspond to B-C boundary in the National Earthquake Hazards Reduction Program (NEHRP) site classification). Therefore, for each of the PBRs, $V_{\text{site}} = 760$ m/s is used. The computed frequency-dependent amplification factors for the precarious rocks thus vary between 1.5 and 2.5.

Overturning Probabilities of PBR Sites

PBRs are effectively low-resolution strong motion seismoscopes that have been operating on solid rock outcrops for thousands of years (Brune, 1996). PBRs give direct indications of the amplitudes of past ground shaking that have not been exceeded during their residence times. The PBRs therefore supply least-upper bounds on the maximum ground-motion values. Since simulated broadband ground motions do not overturn the PBRs with a high probability, the simulated ground motions are not too high. However, the PBRs do not provide information about the expected median amplitudes because the PBRs also would be consistent with no ground motions produced by earthquakes on the San Andreas fault; the PBRs would still be standing in this case. Because the PBRs have been in residence for thousands of years (Bell *et al.* 1998), it is also possible to compare their existences with total seismic hazard estimates (Purvance, Brune *et al.*, 2008). However, in our analysis, we compare the PBRs with ground motions that are consistent with the median values predicted by the GMPEs. Thus, we do not compare the total hazard at the PBR sites but instead examine the PBR response for median ground motions generated for the seven rupture scenarios.

Purvance *et al.* (2008a) found that PBR fragilities are efficiently parameterized via the ground-motion parameters PGA and the ratio PGV/PGA. The PGV/PGA ratio correlates well with the duration or frequency of the predominant acceleration pulse that acts to overturn a PBR. Malhotra (1999) suggests that the PGV/PGA ratio is indicative of strong directivity and demonstrated that it is well correlated with structural damage. High PGV/PGA ratios tend to be measured in areas of high directivity and produce such effects on structures as increasing base shear, interstory drift, and ductility demands. High PGV/PGA ratios may also produce PBR overturning at relatively low PGA amplitudes. PGV/PGA values are generally largest in regions of forward directivity; in these areas, the PGA required for overturning is substantially lower than in areas with low PGV/PGA values. Figure 14 shows the PGV/PGA ratios, highlighting the directivity effect in our broadband simulations. The northwest–southeast scenarios (TS1-2, TS2-3) generate higher ratios in the forward directivity direction (southeast) and significantly lower ratios at near-fault sites in the backward directivity direction (northwest) (e.g., sites S15, S17, S18). The PBR distributions may therefore provide information regarding the rupture orientation, as addressed in Olsen and Brune (2008) based on the low-frequency ground motions only.

The geometrical parameters of the PBRs examined in this study are summarized in Table 2. Purvance *et al.* (2008a) present the method to assess the geometrical parameters, and Purvance, Brune *et al.* (2008) discuss in detail the

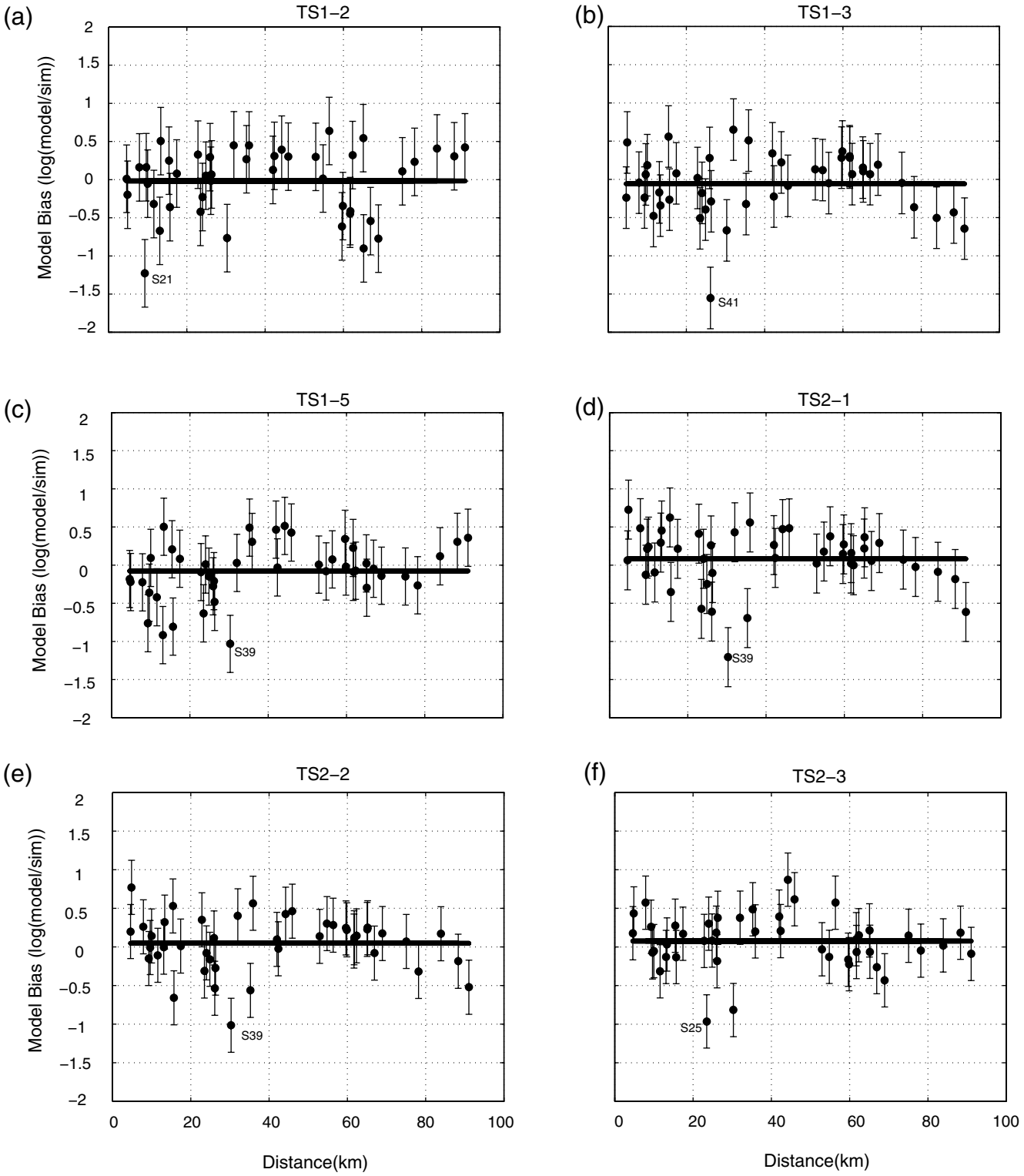

Figure 11. PGA model bias [log (model/sim)] for simulated PGA versus the GMPE of Choi and Stewart (2005) with corresponding uncertainties ($\pm\sigma$) for all sites for each TS scenario: (a) TS1-2, (b) TS1-3, (c) TS1-5, (d) TS2-1, (e) TS2-2, and (f) TS2-3.

uncertainties in these parameters and their effects on the resulting fragility estimates.

We compute the overturning probabilities for three fragility models: -1σ model (more fragile), median rock model (most probable fragility model), and $+1\sigma$ (less fragile) model (see Table 3). We find that the overturning probabilities are ubiquitously zero with the exception of the PBR at S01 (Pioneer Town, all rupture directions), the PBR at S03

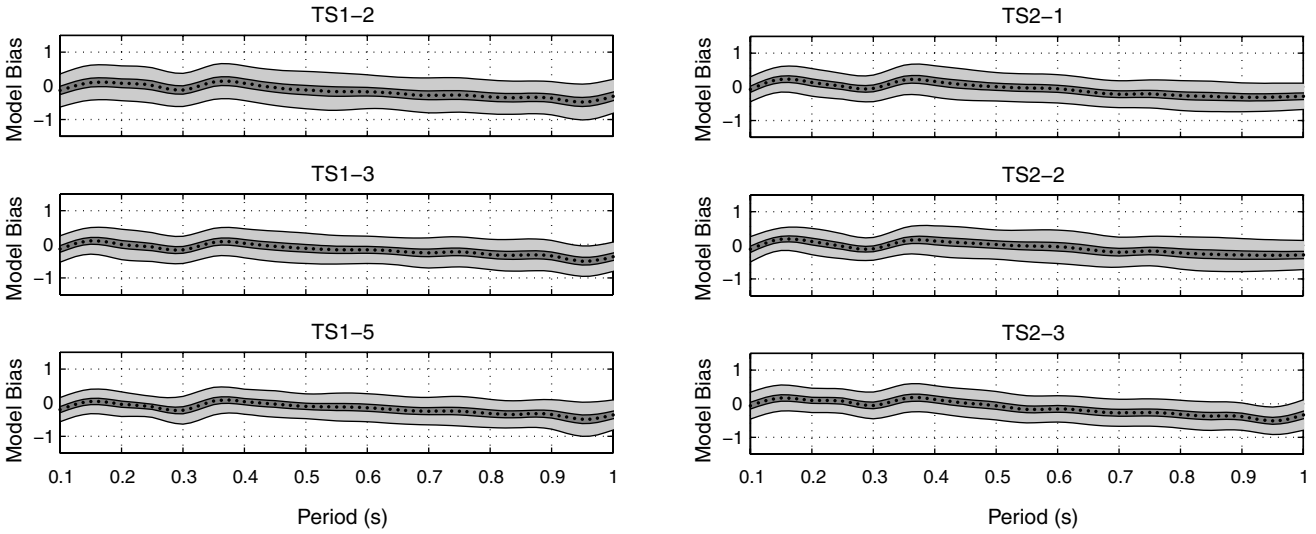

Figure 12. Mean response spectra model bias [log (model/sim)] with corresponding uncertainties ($\pm\sigma$ and 90% confidence intervals), using all stations for individual sites and for ensemble average for each TS scenario: (a) TS1-2, (b) TS1-3, (c) TS1-5, (d) TS2-1, (e) TS2-2, and (f) TS2-3.

(Pinyon Crest, bilateral rupture only), the PBR at S04 (Banning South, bilateral and northwest–southeast rupture directions), the PBR at S05 (Beaumont South, all rupture directions), the PBR at S06 (Tooth, northwest–southeast rupture direction only), and the PBR at S16 (Victorville, southeast–northwest rupture direction only). All of the rupture scenarios produce median overturning probabilities greater than 5% at two or three sites for the median rock model.

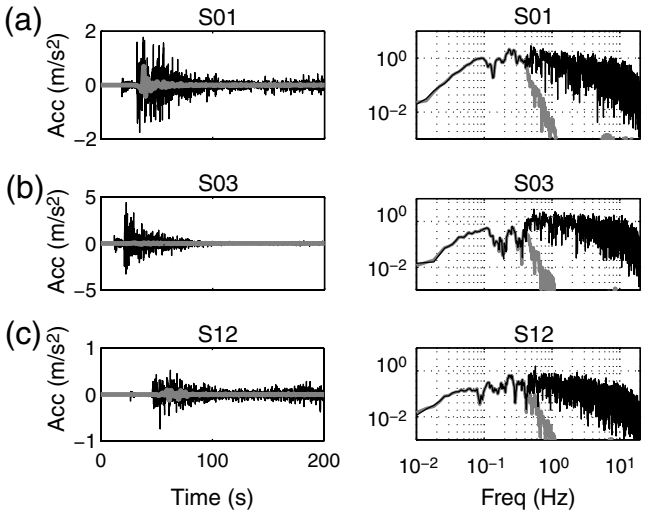

Figure 13. (left) Acceleration time histories and (right) Fourier amplitude spectra at sites (a) S01, (b) S03, and (c) S12 for the TS1-3 scenario. The waveforms and spectra in black are for broadband simulations plotted on the top of the grayish low-frequency synthetics. Station S03 shows some level of mismatch between low-frequency and high-frequency, which results in a discontinuity in the broadband spectra. S01 and S12 are examples where such jumps are not observed.

Discussion and Conclusions

We improved the recently proposed hybrid broadband simulation method of Mai *et al.* (2010) by using dynamically consistent source-time functions and implementing finite-fault effects in the high-frequency wave field for large-magnitude earthquakes. We applied the methodology to seven M_w 7.7 hypothetical earthquakes at 44 rock sites along the San Andreas fault in southern California. The finite-fault effects are implemented following the empirical Green's function method of Irikura (1986), which divides the fault area into a number of subfaults and adds the contributions of each subfault to the total ground motion at the site. Inserting the extended fault geometry as well as the slip variability along the fault incorporates source directivity effects into the high-frequency synthetics. In this study, the scattering Green's functions are efficiently simulated up to 10 Hz, covering the frequency range of general engineering interest.

Sensitivity tests carried out on the scattering parameters (see the Appendix) in the computation of the scattered wave field reveal that a careful selection of the quantities $Q_0 f^n$,κ, η_s, and Nscat is essential as they determine the time domain and spectral properties of the high-frequency synthetics. The sensitivity tests provide guidance for future use of the scattering theory of Zeng *et al.* (1991) in high-frequency ground-motion estimation. We also perform tests to investigate the effect of various source-time functions (simple boxcar and triangular STFs and several dynamically consistent STFs) on the resulting ground motions. While waveforms for different STFs are similar in shape and somewhat different in amplitude, the spectra show significant differences both in shape and amplitude, particularly at frequencies above 1 Hz. The spectra of scatterograms convolved with a Yoffe function demonstrate significant spectral holes at higher

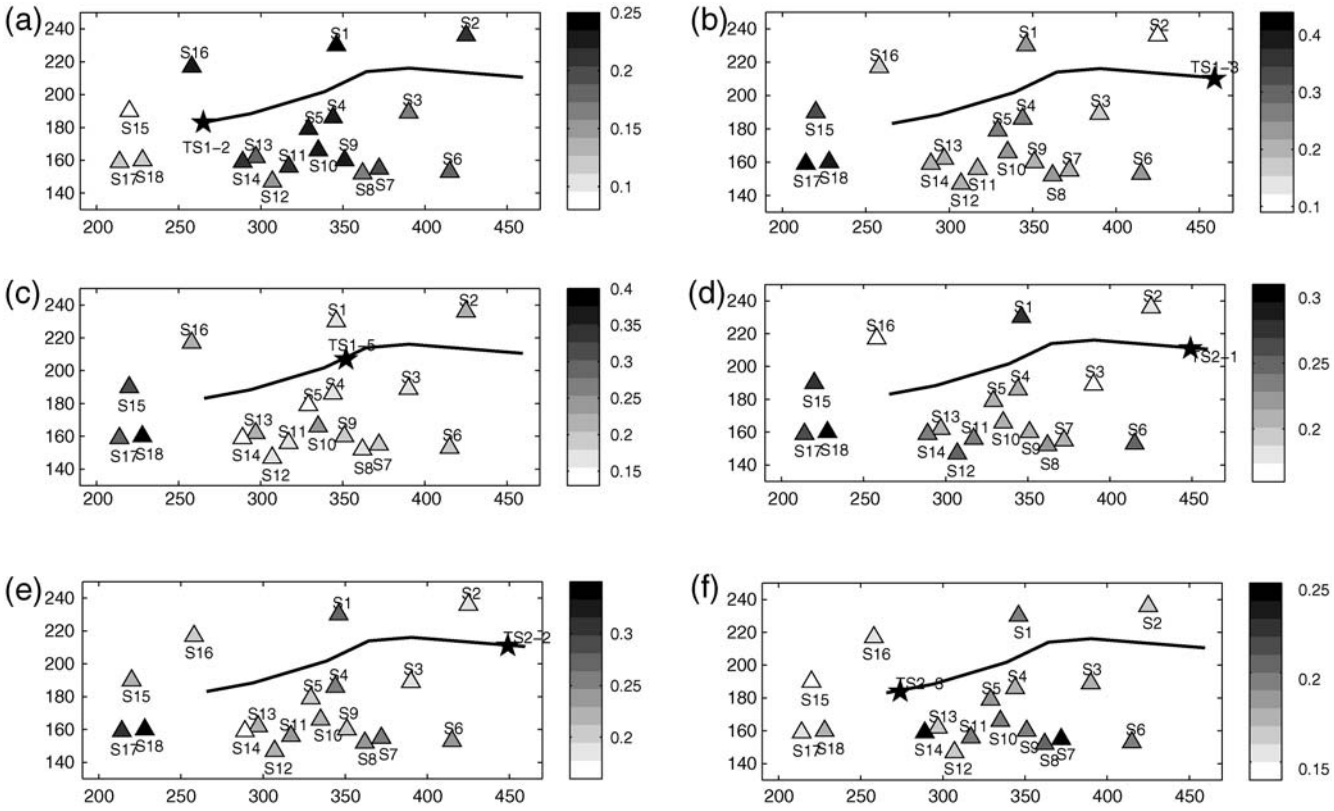

Figure 14. PGV/PGA ratios at the 18 PBR sites calculated for (a) TS1-2, (b) TS1-3, (c) TS1-5, (d) TS2-1, (e) TS2-2, and (f) TS2-3 scenarios. The star on each map shows the epicenter of the corresponding TeraShake scenario.

frequencies. The pulselike STF proposed by Liu *et al.* (2006) generates a scalloped spectral shape in acceleration spectra, continuing with a sharp spectral decay at lower frequencies. The slip-rate function proposed by Dreger *et al.* (2007, Dreger-STF) is favorable because of its well-shaped Fourier spectrum (e.g., no holes in the high-frequency spectra and no sudden fall-off at low frequencies). By adding a healing term into their proposed parameterization as well as a small

Table 2

PBR Geometrical Parameters $\alpha 1$, $\alpha 2$, and p^2 Used in the Overturning Probability Analysis for the 18 PBR Sites in This Study*

ID	Site Name	Longitude	Latitude	$\alpha 1$ (rad)	$\alpha 2$ (rad)	p^2 (1/s)
S01	Pioneer Town	−116.50	34.14	0.2	0.2	24.11417
S02	Cottonwood Springs	−115.81	33.73	0.35	0.35	6.904389
S03	Pinyon Crest	−116.43	33.61	0.3	0.3	12.7
S04	Banning South	−116.82	33.85	0.2	0.24	4.05
S05	Beaumont South	−116.99	33.90	0.3	0.3	14.04345
S06	Tooth	−116.47	33.22	0.19	0.19	8.96
S07	Anza	−116.80	33.48	0.3	0.3	7.021723
S08	Round Top	−116.90	33.52	0.2	0.2	3.601745
S09	Benton Rd.	−116.93	33.59	0.15	0.37	5.44
S10	Nuevo	−117.15	33.78	0.3	0.3	4.45
S11	Perris	−117.24	33.79	0.1	0.45	5.98
S12	Gavilan	−117.36	33.83	0.35	0.35	13.80878
S13	Mockingbird	−117.39	33.88	0.32	0.36	7.21
S14	Pedley	−117.46	33.99	0.38	0.42	14.4
S15	Lovejoy Buttes	−117.83	34.60	0.22	0.24	15.3
S16	Victorville	−117.32	34.57	0.2	0.2	32
S17	Aliso	−118.09	34.42	0.17	0.21	22.3
S18	Pacifico	−117.97	34.35	0.22	0.3	5.88

*See Fig. 1 for locations of PBR sites.

Table 3
PBR Overturning Probabilities (0–1)*

	TS1-2			TS1-3			TS1-5			TS2-1			TS2-2			TS2-3		
Site	-1σ	md	$+1\sigma$	-1σ	md	$+1\sigma$	-1σ	md	$+1\sigma$	-1σ	md	$+1\sigma$	-1σ	md	$+1\sigma$	-1σ	md	$+1\sigma$
S01	0.67	0	0	0.99	0.56	0	0.99	0.62	0.07	0.5	0	0	0.68	0	0	0.89	0.18	0
S02	0.02	0	0	0	0	0	0	0	0	0	0	0	0	0	0	0	0	0
S03	0	0	0	0	0	0	0.36	0.04	0	0	0	0	0.01	0	0	0.03	0	0
S04	0.6	0.13	0	0.35	0	0	0.5	0.12	0	0.21	0	0	0.35	0	0	0.44	0.08	0
S05	0.99	0.92	0.35	0.99	0.99	0.6	0.96	0.34	0.02	0.99	0.72	0.15	0.99	0.94	0.37	0.99	0.6	0.08
S06	0.62	0.1	0	0	0	0	0	0	0	0	0	0	0	0	0	0.04	0	0
S07	0	0	0	0	0	0	0	0	0	0	0	0	0	0	0	0	0	0
S08	0	0	0	0	0	0	0	0	0	0.02	0	0	0	0	0	0.04	0	0
S09	0	0	0	0.23	0	0	0.11	0	0	0.09	0	0	0.08	0	0	0.03	0	0
S10	0	0	0	0	0	0	0	0	0	0	0	0	0	0	0	0	0	0
S11	0.02	0	0	0.01	0	0	0.02	0	0	0.01	0	0	0.01	0	0	0.07	0	0
S12	0	0	0	0	0	0	0	0	0	0	0	0	0	0	0	0	0	0
S13	0	0	0	0.07	0	0	0	0	0	0.03	0	0	0.02	0	0	0	0	0
S14	0	0	0	0	0	0	0	0	0	0	0	0	0	0	0	0	0	0
S15	0	0	0	0	0	0	0	0	0	0	0	0	0	0	0	0	0	0
S16	0	0	0	0.98	0.53	0	0	0	0	0.99	0.98	0.48	0.99	0.98	0.4	0	0	0
S17	0	0	0	0.15	0	0	0	0	0	0	0	0	0	0	0	0	0	0
S18	0	0	0	0	0	0	0	0	0	0	0	0	0	0	0	0	0	0

*The first entries for each scenario in the table are for -1σ model, the second entries are for the median rock model, and the third entries are for $+1\sigma$ model. If the overturning probabilities are zero for all three fragility models, then the probability is shown with one single entry of 0.

amount of random variability, we improved the Dreger-STF to produce acceleration spectra with the desired flat level at high frequencies.

We compare simulated broadband ground-motion amplitudes for the seven TeraShake scenarios with the GMPE of Choi and Stewart (2005) and the more recent NGA GMPE of Campbell and Bozorgnia (2008). The PGA, PGV, and SA values compare favorably with the NGA relations, validating the use of our method for engineering applications. In particular, the comparisons suggest that directivity is correctly accounted for in our broadband method when reasonable choices of the scattering parameters are made. The complexity of the slip distribution (controlling local directivity effects) play an important role in our simulations in generating higher or lower ground motions compared to the GMPEs.

The high-frequency simulation method is computationally inexpensive and, in conjunction with appropriate low-frequency synthetics, efficiently produces ground-motion peak amplitudes in the near-field of large earthquakes that are in good agreement with empirical models. In addition, our strong-motion simulations reflect the ground-motion properties of engineering interest. Therefore, the improved broadband ground-motion simulation methodology is an efficient tool for ground-motion prediction for moderate-size to large-size events. As such, it can be used for various engineering applications, such as performance-based design and nonlinear dynamic analysis (both require full-time history rather than peak amplitudes), as well as for development of new attenuation models or seismic hazard and risk-related studies.

In addition, we compute the overturning probabilities of the 18 PBR sites based on median ensemble PGAs and PGV/PGA ratios. The overturning probabilities at most of the sites are essentially zero (see Table 3) for all seven M_w 7.7 TeraShake scenarios. However, at six sites, one or all of the TeraShake scenarios (northwest–southeast, southeast–northwest, and bilateral rupture directions) produce single-event median overturning probabilities larger than 5%, which for an ensemble of events over the lifetime of the PBRs add up to ensemble values larger than 90% (assuming an exposure to ~67 events during ~10,000 years with an average recurrence period of ~150 years). Based on these results, the PBRs do not favor a preferred rupture direction on the southern San Andreas fault and are inconsistent with repeated exposure to peak ground motions as large as those generated by the M_w 7.7 TeraShake scenarios. As an estimate of the maximum ground-motion level for large earthquakes on the southern San Andreas fault that are consistent with the PBRs, we assume toppling of the PBRs occurs by the median ground motion generating a 50% overturning probability by an ensemble of 60–70 large earthquakes. With these assumptions, the ground motions from the M_w 7.7 TeraShake scenarios need reductions by up to a factor of 2 in order to be consistent with the presence of PBRs (e.g., site S05 for most scenarios). If toppling of the PBR does not occur until exposed to ground motions generating a larger (say, 90%) overturning probability than that assumed previously in this paper (50%), the TeraShake ground motions need reductions less than a factor of 2 in order to be consistent with the PBRs. In any case, the PBRs do not agree with large earthquakes on the southern San Andreas fault, consistently producing

magnitudes much larger than M_w 7.5–7.6 (although a few larger outliers are possible). Our results suggest that the average moment magnitude for large earthquakes on the southern San Andreas fault may be smaller than the M_w 7.7 used for the TeraShake scenarios (which were based on an estimated geological slip rate of ~16 mm/year). Plausible mechanisms accounting for the geological slip rate include redistribution of slip on nearby faults such as the San Jacinto fault and the eastern California shear zone and/or cascades of smaller events ($M_w < 7.5$–7.6) on the southern San Andreas, rather than single large ($M_w > 7.7$) earthquakes. Future work should focus on testing our results, for example using ground-motion synthetics at the PBR sites generated by alternate methods.

Finally note that these results are consistent for both TS1 and TS2 scenarios, suggesting that the bias toward lower PGVs in the Los Angeles basin for ruptures using dynamic rather than kinematic description noted by Olsen *et al.* (2008) does not appear to significantly affect the ground motions at the PBR sites analyzed here. Our results suggest that the speculated preference for bilateral rupture propagation on the southern San Andreas proposed by Olsen and Brune (2008) may have been biased by neglecting the high-frequency ground motions.

Data and Resources

Ground-motion prediction equations used in this paper are calculated using the JavaScript that can be obtained from http://www.opensha.org/ (last accessed March 2009).

The rest of the data used in this paper came from the published sources listed in the references.

Acknowledgments

This study was funded by the Swiss National Science Foundation, Grant 200021-118019, and the Southern California Earthquake Center (SCEC; funded through the National Science Foundation Cooperative Agreement Number EAR-0106924 and U. S. Geological Survey Cooperative Agreement Number 02HQAG0008). This work is SCEC contribution number 1200.

References

Atkinson, G. M., and W. Silva (1997). An empirical study of earthquake source spectra for California earthquakes, *Bull. Seismol. Soc. Am.* **87,** 97–113.

Bell, J. W., J. N. Brune, T. Liu, M. Zreda, and J. C. Yount (1998). Dating precariously balanced rocks in seismically active parts of California and Nevada, *Geology* **26,** 495–498.

Beresnev, I. A., and G. M. Atkinson (1997). Modeling finite-fault radiation from the ω^{-n} spectrum, *Bull. Seismol. Soc. Am.* **87,** 67–84.

Boore, D. M. (1983). Stochastic simulation of high-frequency ground motions based on seismological models of the radiated spectra, *Bull. Seismol. Soc. Am.* **73,** 1865–1894.

Boore, D. M., and J. Boatwright (1984). Average body-wave radiation coefficients, *Bull. Seismol. Soc. Am.* **74,** 1615–1621.

Borcherdt, R. D. (1994). Estimates of site-dependent response spectra for design (methodology and justification), *Earthq. Spectra* **10,** 617–653.

Brune, J. N. (1996). Precariously balanced rocks and ground-motion maps for southern California, *Bull. Seismol. Soc. Am.* **86,** no. 1, 43–54.

Campbell, K. W., and Y. Bozorgnia (2008). NGA ground motion model for the geometric mean horizontal component of PGA, PGV, PGD and 5% damped linear elastic response spectra for periods ranging from 0.01 to 10s, *Earthq. Spectra* **24,** 139–171.

Chandler, A. M., N. T. K. Lam, and H. H. Tsang (2006). Near-surface attenuation modeling based on rock shear wave velocity profile, *Soil Dynam. Earthq. Eng.* **26,** no. 11, 1004–1014.

Choi, Y., and P. S. Stewart (2005). Nonlinear site amplification as a function of 30m shear wave velocity, *Earthq. Spectra* **21,** no. 1, 1–30.

Dreger, D., E. Tinti, and A. Cirella (2007). Slip velocity function parameterization for broadband ground motion simulation, *Seismological Society of America 2007 Annual Meeting* Waikoloa, Hawaii, 11–13 April 2007.

Gottschämmer, E., and K. B. Olsen (2001). Accuracy of the explicit planar free surface boundary condition implemented in a fourth-order staggered-grid velocity-stress finite-difference scheme, *Bull. Seismol. Soc. Am.* **91,** 617–623.

Graves, R., and A. Pitarka (2004). Broadband time history simulation using a hybrid approach, paper 1098, *Thirteenth World Conf. on Earthquake Engineering, Conference Proceedings*, Vancouver, British Columbia, 1–6 August 2004.

Guatteri, M., P. M. Mai, and G. C. Beroza (2004). A pseudo-dynamic approximation to dynamic rupture models for strong ground motion prediction, *Bull. Seismol. Soc. Am.* **94,** 2051–2063.

Guatteri, M., M. P. Mai, G. C. Beroza, and J. Boatwright (2003). Strong motion prediction from stochastic-dynamic source models, *Bull. Seismol. Soc. Am.* **93,** 301–313.

Hartzell, S., M. Guatteri, P. M. Mai, P. Liu, and M. Frisk (2005). Calculation of broadband time histories of ground motion, Part II: Kinematic and dynamic modeling using theoretical Green's functions and comparison with the 1994 Northridge earthquake, *Bull. Seismol. Soc. Am.* **95,** 614–645.

Hartzell, S., S. Harmsen, A. Frankel, and S. Larsen (1999). Calculation of broadband time histories of ground motion: Comparison of methods and validation using strong-ground motion from the 1994 Northridge earthquake, *Bull. Seismol. Soc. Am.* **89,** 1484–1504.

Hole, J. A. (1992). Non-linear high resolution three-dimensional seismic travel time tomography, *J. Geophys. Res.* **97,** 6553–6562.

Husid, R. L. (1969). Analisis de terremotos: Analisis General, *Revista del IDIEM* **8,** 21–42, Santiago, Chile (in Spanish).

Irikura, K. (1986). Prediction of strong acceleration motions using empirical Green's function, in *Proc. 7th Japan Earthq. Eng. Symp.* 151–156, Tokyo, Japan. 10–12 December 1986.

Irikura, K., and K. Kamae (1994). Estimation of strong ground motion in broad-frequency band based on a seismic source scaling model and an empirical Green's function technique, *Ann. Geofis.* **37,** 1721–1744.

Kamae, K., K. Irikura, and A. Pitarka (1998). A technique for simulating strong ground motion using hybrid Green's function, *Bull. Seismol. Soc. Am.* **88,** 357–367.

Kohler, M. D., H. Magistrale, and R. W. Clayton (2003). Mantle heterogeneities and the SCEC reference three-D seismic velocity model version 3, *Bull. Seismol. Soc. Am.* **93,** 757–774.

Liu, P., R. A. Archuleta, and S. H. Hartzell (2006). Prediction of broadband ground-motion time histories: Hybrid low/high-frequency method with correlated random source parameters, *Bull. Seismol. Soc. Am.* **96,** no. 6, 2118–2130.

Magistrale, H., S. M. Day, R. Clayton, and R. W. Graves (2000). The SCEC southern California reference three-dimensional seismic velocity model version 2, *Bull. Seismol. Soc. Am.* **90,** 65–76.

Mai, P. M., and G. C. Beroza(2003). A hybrid method for calculating near-source, broadband seismograms: Application to strong motion prediction, *Phys. Earth Planet. Int.* **137,** no. 1–4, 183–199.

Mai, P. M., W. Imperatori, and K. B. Olsen (2010). Hybrid Broadband Ground-Motion Simulations: Combining Long-Period Deterministic

Synthetics with High-Frequency Multiple S-to-S Backscattering, *Bull. Seis. Soc. Am.* **100**, no. 5A, 2124–2142.
Malhotra, P. K. (1999). Response of buildings to near-field pulse-like ground motions, *Earthq. Eng. Struct. Dynam.* **28,** 1309–1326.
Marcinkovich, C., and K. B. Olsen (2003). On the implementation of perfectly matched layers in a 3D fourth-order velocity-stress finite-difference scheme, *J. Geophys. Res.* **108,** no B5, 2276.
Mena, B., E. Durukal, and M. Erdik (2006). Effectiveness of hybrid Green's function method in the simulation of near-field strong motion: An application to the 2004 Parkfield earthquake, *Bull. Seismol. Soc. Am.* **96,** 183–205.
Oglesby, D. D., D. S. Dreger, R. Harris, N. Ratchkovski, and R. Hansen (2004). Inverse kinematic and forward dynamic models of the 2002 Denali, Alaska earthquake, *Bull. Seismol. Soc. Am.* **94,** S214–S233.
Olsen, K. B. (1994). Simulation of three-dimensional wave propagation in the Salt Lake Basin, *Ph.D. Thesis*, University of Utah, Salt Lake City, Utah, 157 p.
Olsen, K., and J. Brune (2008). Constraints from precariously balanced rocks on preferred rupture directions for large earthquakes on the southern San Andreas fault, *J. Seismol.***12,** no. 2, 235–241.
Olsen, K. B., S. M. Day, J. B. Minster, Y. Cui, A. Chourasia, M. Faerman, R. Moore, P. Maechling, and T. Jordan (2006). Strong shaking in Los Angeles expected from southern San Andreas earthquake, *Geophys. Res. Lett.* **33,** L07305, doi 10.1029/2005GL025472.
Olsen, K. B., S. M. Day, J. B. Minster, Y. Cui, A. Chourasia, D. Okaya, P. Maechling, and T. Jordan (2008). TeraShake2: Simulation of M_w 7.7 earthquakes on the southern San Andreas with spontaneous rupture description, *Bull. Seismol. Soc. Am.* **98,** 1162–1185.
Peyrat, S., K. B. Olsen, and R. Madariaga (2001). Dynamic modeling of the 1992 Landers earthquake, *J. Geophys. Res.* **106,** 26467–26482.
Pitarka, A., P. Somerville, Y. Fukushima, T. Uetake, and K. Irikura (2000). Simulation of near fault strong ground motion using hybrid Green's functions, *Bull. Seismol. Soc. Am.* **90,** 566–586.
Pulido, N., and T. Kubo (2004). Near-fault strong motion complexity of the 2000 Tottori earthquake (Japan) from a broadband source asperity model, *Tectonophysics* **390,** 177–192.
Pulido, N., and M. Matsuoka (2006). Broadband strong motion simulation of the 2004 Niigata-ken Chuetsu earthquake: Source and site effects, *Third International Symposium on the Effects of Surface Geology on Seismic Motion*, Grenoble, France, 1**,** 657–666.
Purvance, M. D., A. Anooshehpoor, and J. N. Brune (2008a). Freestanding block overturning fragilities: Numerical simulation and experimental validation, *Earthq. Eng. Struct. Dynam.* **37,** 791–808.
Purvance, M. D., A. Anooshehpoor, J. N. Brune, and R. E. Abbot (2008b). Site conditions at precariously balanced rock (PBR) sites in Mojave, southern California, *Seismological Society of America 2008 Annual Meeting*, Santa Fe, California, 16–18 April 2008.
Purvance, M. D., J. N. Brune, N. A. Abrahamson, and J. G. Anderson (2008). Consistency of precariously balanced rocks with probabilistic seismic hazard estimates in southern California, *Bull. Seismol. Soc. Am.* **98,** 6.
Raoof, M., R. B. Herrmann, and L. Malagnini (1999). Attenuation and excitation of three-component ground motion in southern California, *Bull. Seismol. Soc. Am.* **89,** no. 4, 888–902.
Rodgers, A., N. A. Petersson, S. Nilsson, B. Sjögreen, and K. McCandless (2008). Broadband waveform modeling of moderate earthquakes in the San Francisco Bay area and preliminary assessment of the USGS 3D seismic velocity model, *Bull. Seismol. Soc. Am.* **98,** 969–988.
Sieh, K., and P. Williams (1990). Behaviour of the southernmost San Andreas fault during the past 300 years, *J. Geophys. Res.* **95,** 6629–6645.
Somerville, P., K. Irikura, R. Graves, S. Sawada, D. Wald, N. Abrahamson, Y. Iwasaki, T. Kagawa, N. Smith, and A. Kowada (1999). Characterizing crustal earthquake slip models for the prediction of strong ground motion, *Seismol. Res. Lett.* **70,** 59–80.
Tinti, E., E. Fukuyama, A. Piatanesi, and M. Cocco (2005). A kinematic source-time function compatible with earthquake dynamics, *Bull. Seismol. Soc. Am.* **95,** no. 4, 1211–1223.
Travasarou, T. (2003). Optimal ground motion intensity measures for probabilistic assessment of seismic slope displacement. *Ph.D. Thesis*, University of California at Berkeley.
Trifunac, M. D., and A. G. Brady (1975b). A study of the duration of strong earthquake ground motion. *Bull. Seismol. Soc. Am.* **65,** 581–626.
Working Group on California Earthquake Probabilities (1995). *Bull. Seismol. Soc. Am.* **85,** 379–439.
Zeng, Y. H., K. Aki, and T. L. Teng (1993). Mapping of the high-frequency source radiation for the Loma Prieta earthquake, California, *J. Geophys. Res.* **98,** no. B7, 11981–11993.
Zeng, Y. H., J. G. Anderson, and F. Su (1995). Subevent rake and random scattering effects in realistic strong ground motion simulation, *Geophys. Res. Lett.* **22,** no._1, 17–20.
Zeng, Y. H., F. Su, and K. Aki (1991). Scattering wave energy propagation in a random isotropic scattering medium 1. Theory, *J. Geophys. Res.* **96,** no. B1, 607–619.

Appendix

Sensitivity Study of Scattering Parameters

To examine how particular choices of the scattering parameters affect the broadband ground motions, we conduct a detailed sensitivity study by varying the following parameters: scattering coefficient (elastic attenuation), η_s; frequency-dependent quality factor (anelastic attenuation), $Q_0 f^n$; site kappa, κ; and the number of elementary scatterers, Nscat. By changing one parameter at a time and fixing the random seed number for generating the incoherent coda waves; we measure the variation in several strong motion parameters: peak ground acceleration, PGA; strong motion duration, SMD; Arias intensity, AI; and high-frequency spectral decay, n. SMD significantly influences structural damage and soil response (Trifunac and Brady, 1975) and is computed as the time interval over which 5% to 95% of the total wave energy is accumulated (Husid, 1969). AI is a ground-motion parameter that captures the potential destructiveness of an earthquake as the integral of the squared acceleration time history and includes the effects of both amplitude and frequency content of a strong motion record. It is a widely used intensity measure in the engineering community because it correlates well with commonly used demand measures of structural response. In addition, AI is also a good predictor of the displacement response of engineering structures (Travasarou, 2003). The spectral parameters defining the spectral shape, peak amplitude, and ω^{-n} are also measured by performing a spectral fit to acceleration spectra.

Various sites among the 18 PBR locations have been used for the sensitivity tests. For brevity, we only show the sensitivity plots for station S11. The sensitivity of ground-motion parameters to the scattering coefficient, η_s, is illustrated in Figure A1. η_s is critical for determining the time domain characteristics of ground motion since it controls the coda envelope (equations. 1, 2). Increasing η_s between $0.002 \leq \eta_s \leq 0.05$ km^{-1} (chosen based on the values η_s tested in Zeng *et al.*, 1991) causes a slower *S*-wave coda decay and therefore produces increasing SMD, as well as increasing PGA and AI. Figure A1 shows that SMD

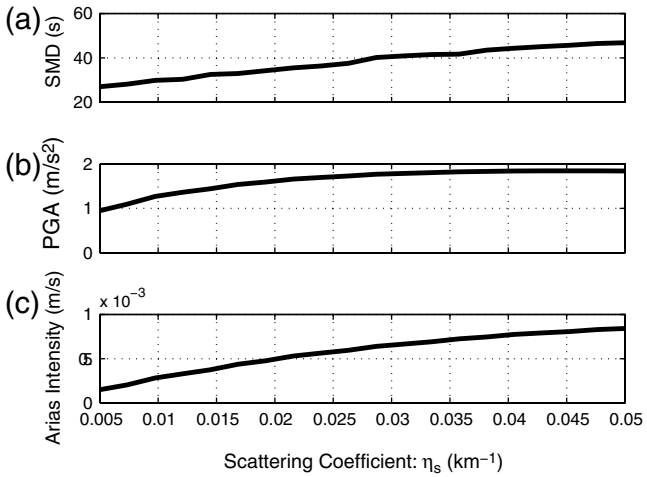

Figure A1. Sensitivity of ground-motion parameters to the scattering coefficient (η_s): (a) SMD (s); (b) PGA (m/s^2); and (c) AI (m/s).

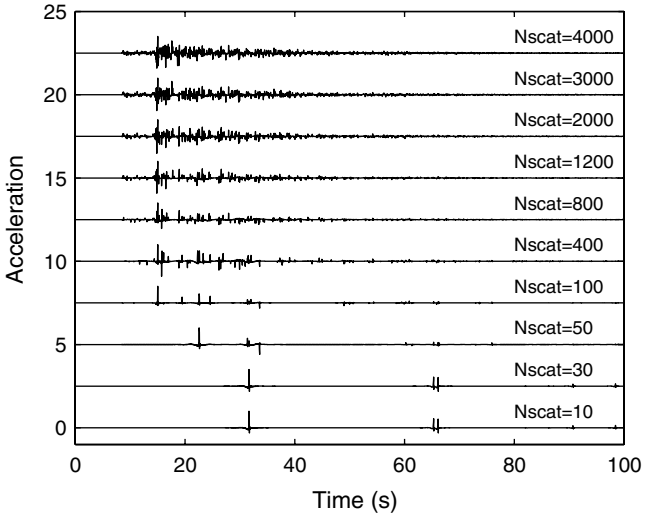

Figure A3. Scattering Green's functions generated for different number of scatterers (Nscat), with Nscat increasing from bottom to top.

changes from 25 up to 45 s. For $\eta_s \geq 0.05$, the changes in ground-motion parameters are insignificant; η_s is subsequently drawn from a uniform distribution where $0.005 \leq \eta_s \leq 0.05$ with a standard deviation of 0.005.

Estimates of frequency-dependent path attenuation ($Q(f) = Q_0 f^n$) are available from the literature for southern California earthquakes. For example, Raoof *et al.* (1999) derived $Q(f) = 180f^{0.45}$, while Atkinson and Silva (1997) developed a regional attenuation model $Q(f) = 150f^{0.6}$. In our simulations, the chosen attenuation model enters into the calculations of the scattering Green's function, while the final high-frequency scatterogram is obtained by convolving this scattering Green's function with the selected slip-rate function. Because the slip-rate functions exhibit a spectral decay of roughly $1/f$ (with minor frequency dependence, see Fig. 2c), the frequency-decay parameter for the scattering Green's function needs to be chosen such that the final broadband velocity amplitude spectra decay as $\sim 1/f$. Using this latter constraint, we find that applying an attenuation model of the form $Q(f) = 150f^{0.8}$ for the scattering calculations, along with the Dreger-STF, provide a $1/f$ frequency decay of velocity-amplitude spectra and a flat acceleration spectra out to ~20 Hz. We therefore use this relation in the subsequent computation of the high-frequency scatterograms for the TeraShake simulations. Note however, that the values of Q_0 and n for the relation $Q_0 f^n$ in our method depend on the choice of source-time function and, for that reason, cannot be compared to other published attenuation models.

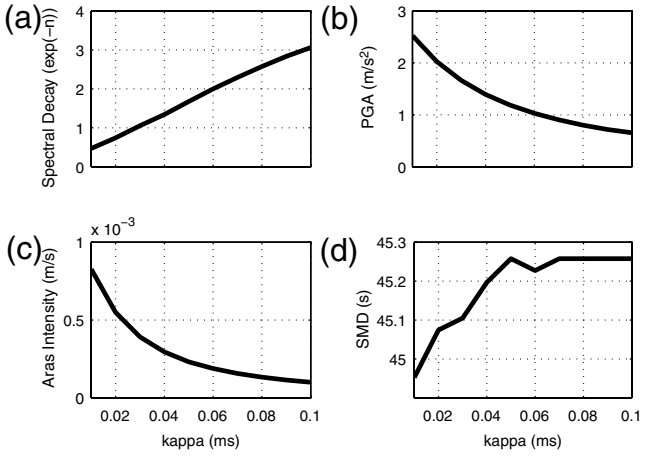

Figure A2. Sensitivity of ground-motion parameters to site kappa. Effect of kappa on (a) the power n of the spectral decay ω^{-n}, (b) PGA (m/s^2), (c) AI (m/s), and (d) SMD (s).

κ is the site-specific high-frequency attenuation (e.g., path independent diminution) that mainly controls the high-frequency decay of the spectrum. κ has a significant effect on the high-frequency spectral decay (ω^n) of the scattering Green's function (Fig. A2a) and therefore also affects PGA. Varying κ from 0.01 to 0.1 decreases the PGA values by a factor of about 2.5 (Fig. A2b). Because AI is obtained by integration of squared acceleration over the duration, AI is also sensitive to the choice of kappa (κ) (Fig. A2c). SMD is insensitive to κ (Fig. 6d; SMD changes only between 45–45.3 s for different values of κ). Chandler *et al.* (2006) computed $\kappa = 0.04$ ms for generic rocks in southern California. However, precarious rock sites are more sensitive to high frequencies than an average site with this generic κ-value, meaning that $\kappa = 0.04$ ms may attenuate high frequencies more strongly than appropriate (Purvance *et al.*, 2008b). We find that $\kappa = 0.03$ ms generate a good fit between the broadband synthetics and GMPEs for the 18 PBR sites.

Scattering Green's functions for different numbers of elementary scatterers (Nscat) are illustrated in Figure A3.

The sensitivity to Nscat is low for values above 1200 but considerable for Nscat below a few hundred. Nscat $\geq$ 1200 shows stable waveforms, while a small number of scatterers (Nscat $\leq$ 400) are insufficient for high-frequency simulation. Few scatterers may be appropriate in cases in which short subfault-specific scattering wavelets are needed. For the high-frequency TeraShake simulations shown in this study, we used Nscat = 1500.

Finally an additional sensitivity test is carried out to demonstrate how different random realizations for the scattering Green's function (generated with different random seed numbers but identical scattering parameters) affect ground-motion values. We find that PGVs and PGAs vary about 10% depending on different random-media parameterizations, demonstrating that the effects of the random seed values are rather small (for detailed test see Mai *et al.* (2010)). This level of uncertainty will be insignificant in the logarithmic attenuation comparison plots.

Institute of Geophysics
ETH Zurich
Sonneggstr. 5, NO H39.2, 8092
Zürich, Switzerland
banu.sanli@sed.ethz.ch
(B.M., P.M.M.)

Deptartment of Geological Sciences
MC-1020
5500 Campanile Dr.
San Diego State University
San Diego, California 92182-1020
(K.B.O.)

Seismological Laboratory
University of Nevada
Reno, Nevada 89557
(M.D.P., J.N.B.)

Manuscript received 28 October 2008